Fracture behavior of brittle particulate composites consisting of a glass matrix and glass or ceramic particles with elastic property mismatch

Tanguy Lacondemine, Julien Moriceau, Theany To, Patrick Houizot, Fabrice Célarié, Dusan Galusek, Jozef Kraxner, Marion Vandenhende, Gaëlle Delaizir, Raphael Langlois, et al.

Fracture behavior of brittle particulate composites consisting of a glass matrix and glass or ceramic particles with elastic property mismatch

Tanguy Lacondemine[a], Julien Moriceau[a], Theany To[a], Patrick Houizot[a], Fabrice Célarié[a], Dusan Galusek[b], Jozef Kraxner[b], Marion Vandenhende[c], Gaëlle Delaizir[c], Raphael Langlois[d], Julien Réthoré[d], Jérôme Adrien[e], Eric Maire[e], and Tanguy Rouxel[a, f]

[a]Mechanics and Glass Department, Institut de Physique de Rennes (IPR), UMR CNRS 6251, Campus de Beaulieu, 35042 Rennes cedex, France

[b]Centre for Functional and Surface Functionalized Glass, Alexander Dubček University of Trenčín, 91150 Trenčín, Slovakia

[c]Institut de Recherche sur les Céramiques (IRCER), UMR CNRS 7315, Université de Limoges, Centre Européen de la Céramique, 87068 Limoges, France

[d]Nantes Université, Centrale Nantes, CNRS UMR 6183, GeM, 44321 Nantes Cedex 3, France

[e]MATEIS, INSA Lyon, UMR CNRS 5510, 69621 Villeurbanne Cedex, France

[f]Institut Universitaire de France, Paris, France

Corresponding author: Tanguy Rouxel, tanguy.rouxel@univ-rennes.fr

---

ABSTRACT — The aim of this work is two-fold: i) elaborating dense and transparent inorganic glass composites with improved fracture properties, and ii) testing the theoretical analysis proposed in [1] and based on Poisson's ratio mismatch. Particulate composites, consisting of glass or ceramic particles embedded in a soda-lime-silica glass matrix, were synthesized and their fracture behavior was studied by means of the Single Edge Precraked Beam (SEPB) and Double Cantilever Drilled (DCDC) methods, using in situ experiments with X-ray tomography where possible. An important effect of the T-stress on the fracture toughness (K_{Ic}) was observed in the case of DCDC exdperiments. K_{Ic} is increased by about 40 % by incorporating 7 vol. % amorphous silica beads or $SrAl_2O_4$:Eu,Dy ceramic particles (SAED) with a 40 μm mean particle size. It is suggested that toughening results from the crack front trapping and pinning at particle sites and from the tortuous crack path in the case of a-SiO_2 particles, and from the contribution of the intrinsic fracture surface energy of the ceramic particles, which are cleaved by the propagating crack, in the case of the SAED particles. The thermally induced stress field is believed to play a major role in the case of a-SiO_2 particles. Two glass grades possessing Young's moduli similar to the one of the matrix but much larger Poisson's ratios were used to produce glass beads. However, the incorporation of these latter beads in the matrix was found to have a minor incidence on the fracture behavior.

Keywords: Crack propagation; Brittle fracture; Glass matrix composites; Digital image correlation; Toughness

1. Introduction

This study is motivated on the one hand, by the search for synthesis methods and shaping parameters making it possible to obtain centimeter-sized transparent composites made up of a glass matrix and glass particles, and on the other hand to explore the impact of differential physical properties on cracking behavior.

The incorporation of glass inclusions in a glass matrix is of great interest to introduce some new functionalities (electrical, magnetic, optical, etc.) in a glass while maintaining the transparency, and to improve the mechanical performance through composite effects. We have shown in a

previous theoretical work focusing on the modeling of the microcracking behavior of glass matrix / glass particles composites [1] that even in the case where both phases share the same Young's modulus value (E), differences in Poisson's ratio (ν) give birth to second-order stresses on mechanical loading, which result in interesting changes in the fracture properties. The appearance of second-order stresses upon mechanical loading can be understood from the way a particle loaded in tension deforms depending on its Poisson's ratio, as is illustrated in Fig. 1a,b. A strong dependence of the crack path on ν was brought to light. A propagating crack tends to be attracted toward inclusions and crack front pinning and bridging phenomena are predicted in the case of adhesive inclusions with $\nu_i < \nu_m$, where subscripts "i" and "m" stand for inclusions and matrix respectively. If the crack further propagates through the particles, the intrinsic fracture toughness of the latter comes into play in the reinforcement. On the contrary, if $\nu_m < \nu_i$, a propagating crack is expected to be twisted around — and deflected by — the inclusions, resulting in a tortuous fracture path, while there is no direct contribution of the fracture properties of the second phase to the fracture behavior of the composite. A significant influence on the fracture toughness in the case where $\nu_i < \nu_m$ and a very limited one in the opposite case were also anticipated. These predictions are schematically summarized in Fig. 1c-d. Nevertheless, in such composites, the build-up of thermally induced residual stresses upon cooling due to the thermal expansion mismatch between the inclusion and the matrix and to the inability of the glass to relax stresses viscoelastically at a temperature below T_g, is mostly unavoidable. The incidence of the corresponding stress field on the crack path and on the stress intensity factor along the crack front is characterized and discussed case by case.

Glass offers a unique opportunity to vary the chemical compositions and the physical properties in a continuous manner so as, for example, to cover wide ranges of elastic characteristics. In the case of inorganic glasses, E and ν range from a few GPa to about 200 GPa and from 0.1 to 0.4, respectively, depending on the chemical system [2]. In the present study, four glass grades with relatively similar Young's moduli, within the 67-77 GPa interval, but with very different values for Poisson's ratio, from 0.15 to 0.29, were synthesized and used either as a matrix or as inclusions. The selected compositions are shown in Fig. 2.. The preparation of homogeneous glass beads (spherical inclusions), large enough to ease the dispersion in the matrix, and the processing of dense and homogeneous composites, large enough to fabricate centimeter-sized test pieces suitable to the fracture experiments, is a very challenging task, which is described in the next paragraph. Then, fracture toughness and fracture surface energy were determined by means of the Single Edge Precracked Beam method (SEPB). Finally, in order to follow the crack path in-situ and to favor a stable crack extension, double cleavage drilled compression tests (DCDC) were carried out, and post-mortem fracture surfaces were characterized. Some DCDC experiments were conducted in situ in a X ray tomograph, which allows to obtain volume information on the crack front geometry and on the crack-particles interactions. The crack geometry was also investigated at the surface and in the volume by means of Digital Image Correlation (DIC) and Digital Volume Correlation (DVC), which allowed to determine the stress intensity factor along the crack front during propagation.

2. Materials

2.1 Glass matrices

Four glass grades were selected for this study, namely, in order of increasing ν values, an amorphous silica glass, a-SiO_2 (Saint-Gobain Comp., Vitreosil® 055, $\nu \approx 0.16$), a soda-lime-silica glass (Saint-Gobain Comp., Planilux, $\nu \approx 0.23$), having a typical window glass composition, $(Na_2O)_{13.4}(CaO)_{9.6}(MgO)_4(Al_2O_3)_{0.6}(SiO_2)_{72}$, referred to as WG, a zinc barium borate glass, $(ZnO)_{20}(BaO)_{20}(B_2O_3)_{60}$ ($\nu \approx 0.28$), referred to as BZBa, and a barium aluminosilicate glass, $(SiO_2)_{58.2}(BaO)_{38.8}(Al_2O_3)_3$ ($\nu \approx 0.29$), referred to as B_2S_3 [3]. The last

two grades were synthesized by the classical melting-quenching-annealing method, starting from high purity SiO_2, $BaCO_3$, Al_2O_3, ZnO, and H_3BO_3 powders (Sigma Aldrich corp., purity > 99.5 %). The powder mixtures were heated in a platinum-rhodium (10 %) crucible up to 1100 °C and 1500 °C (T_{max}) for the BZBa and the B_2S_3 grades, respectively. The melt was homogenized for one hour at T_{max} and then quenched in ambient atmosphere, by pouring the glass into a nickel super-alloy mold. The obtained glass was crushed in an agate mortar and remelted twice to improve the chemical homogeneity. In addition, commercially available particles made of strontium aluminate doped with europium and dysprosium, $SrAl_2O_4$:Eu,Dy (Sigma Aldrich corp.), referred to as SAED, about 40 to 50 µm in size, were used as a second phase to make a glass matrix / ceramic particles composites. This latter composite material was developed in a previous work to produce a mechanoluminescent glass-matrix composite. Details regarding the processing of this composite can be found in ref. [4]. In the end, the four glasses were available as powders to be used as matrix. Some physical properties of the glass grades are given in Table 1, together with the properties of the SAED ceramic.

2.2 Glass beads

We aimed at producing composites with spherical reinforcements. Nearly spherical and homodispersed a-SiO_2 beads, ≈ 450 nm in diameter, were first obtained by means of a Ströber type sol-gel route [5]. However, such small particles tend to agglomerate and were found to dissolve in the glass melt, making it impossible to fabricate the composite materials by direct incorporation of the beads in the melt and further homogenization using a platinum mixing tool. Therefore, glass beads of a-SiO_2 and BZBa compositions were synthesized by means of a flame synthesis method, allowing for the synthesis of beads, 30 to 100 µm in diameter. In this technique, a glass precursor (glass particles) is fed to a gas torch with a maximum temperature of flame up to 2200 °C, yielding to molten glass (liquid) droplets, which further experience a rapid cooling at a rate as large as – 1000 °C·s^{-1}, allowing the production of microspheres, which are fully amorphous, thanks to the high cooling rate and to the fact that this is a contactless technique [6]. Examples of glass beads obtained in this study are shown in Fig. 3. Amorphous silica being remarkably refractory, it turns out that precursor particles smaller than 50 µm only gave rise to spherical beads. Larger glass spheres, up to 100 µm, were obtained with the BZBa grade. Beads were further sifted so as to get a size distribution for the four different glass grades within 25-50 µm, with a mean size of about 30 µm.

2.3 Composites

Glass matrix / glass beads composites with different fractions of beads, up to 10 vol. % (7 vol. % will be chosen afterward), were synthesized by mixing matrix powders and reinforcement spheres together and subsequent sintering by means of a spark plasma sintering (SPS) technique using a a Dr.Sinter 825 Syntex machine. The powders were inserted in a graphite die and consolidated at a temperature close to the T_g of the glass matrix for few minutes and under a 50 MPa uniaxial pressure. WG, BZBa and B_2S_3 grades were first considered as matrices and as second phase particles as well, while a-SiO_2 was solely used as inclusions. However, it turned out that when BZBa and B_2S_3 are used as matrices, the particles obtained by crushing bulk glass batches tended to agglomerate. WG was thus finally regarded as the most suitable material for the matrix. In a preliminary step, the sintering behavior of the glass matrix was studied and optimized so as to get dense and transparent materials. For this purpose, the glass was crushed in an agate mortar so as to obtain a glass powder with an average particle size of 150 µm. Note that the role of the glass matrix particle size was investigated for three powders with grain size distributions centered on 38, 75 and 150 µm, and it turned out that the larger the particle size is and the more transparent the sintered glass becomes. This is because small particles result in finer and more numerous pores, which promote carbon contamination during spark-plasma

sintering [7,8]. Pellets, 10 mm in diameter and 3 mm in thickness, were prepared from the 150 µm powder grade by cold pressing under a pressure of about 400 MPa. The onset for sintering was investigated by thermal expansion experiments and a pre-sintering heat-treatment of the pellets at ~ T_g+70 °C for 20 min was carried out in order to reduce the contamination by graphite in the SPS chamber during the sintering treatment, which is in turn performed at ~T_g+30 °C for about 2 min under a uniaxial pressure of 64 MPa.

The second step consists in incorporating the glass beads in the glass matrix powder to obtain a dry powder mixture that is homogenized in a shaker-mixer (turbula) for 45 min. A uniform dispersion of the second phase spheres was reached most cases and the sintered pellets were mostly transparent as long as the second phase volume fraction did not exceed 2 vol. %. Nevertheless, dense, homogeneous and mostly translucent composite materials were obtained for fraction of beads up to 7 vol. % (Fig. 4). A volume fraction of 7 % was thus chosen for this study. We observed that for the chosen dispersion means (dry mixing in a turbula), 7 vol. % of the second phase is a maximum because the dispersion becomes less effective at larger content. Particle agglomeration is already visible (but relatively limited) in the cases of the WG / a-SiO_2 and WG / B_2S_3 composites (Figs 4e and 4f). There is certainly room for improvement in the dispersion process. A major difficulty of the preparation of specimens for mechanical testing lies in the fact that it requires an upscaling from the 10 mm large pellets to over 50 mm large disks. Lengthy investigations aimed at adjusting the pre-sintering and SPS cycles were necessary for each matrix / beads couple. Some physical properties of interest for the present study are given in Table 2. The maximum hydrostatic pressure (P) induced in the inclusions upon cooling from the sintering temperature (ΔT= –544 °C) due to thermal expansion coefficient mismatch between the matrix and the inclusions, and the critical particle size, R_c, that would result in microcracking of the matrix upon cooling due to the thermally-induced residual stress field are also given in Table 2. Values for P and R_c were obtained by means of the expressions proposed by Selsing [9] and Davidge et al. [10] respectively:

$$P = \frac{(\alpha_m - \alpha_i)\Delta T}{\frac{1+\nu_m}{2E_m} + \frac{1-2\nu_i}{2E_i}} \quad (1)$$

$$R_c = \frac{8\gamma_m}{\left[\frac{1+\nu_m}{E_m} + \frac{2(1-2\nu_i)}{E_i}\right] P^2} \quad (2)$$

where γ_m is the fracture surface energy of the matrix and is close to 3.55 J·m^{-2} for the soda-lime-glass (WG) chosen for this study [11]. Values for P and R_c will be discussed in section 4.

3. Experimental methods

3.1 Physical and thermal properties

The specific mass (ρ) was measured by the Archimedes' method in distilled water at 20 °C. Data for ρ were averaged on five measurements. The linear thermal expansion coefficient (α) was determined by dilatometry on 6×4×4 mm^3 specimens, with a heating rate of 10 °C·min^{-1}. The glass transition temperature (T_g) was taken as the intersection of straight lines fitting the data corresponding to the supercooled liquid and the glassy ranges (a smooth fit was observed over 50 °C in the supercooled liquid domain and over 400 °C in the glassy one). The refractive index at 633 nm was measured by means of a Metricon 2010/M apparatus (Metricon Corp., USA).

3.2 Mechanical properties

All measurements were carried out in a room at 20 °C with 60 % humidity (controlled atmosphere).

The elastic moduli of the parent bulk glasses used for particle manufacturing were measured by means of ultrasonic echography using 10 MHz piezoelectric transducers. In this measurement, velocities of longitudinal (V_L) and transverse (V_T) waves were calculated from the sample thickness (L) and transit time (τ). Young's modulus (E) and shear modulus (G) were then obtained by means of Eq. (3) and Eq. (4), respectively, and Poisson's ratio (v) is further derived by means of Eq. (5):

$$E = \rho \frac{3V_L^2 - 4V_T^2}{(V_L/V_T)^2 - 1} \quad (3)$$

$$G = \rho V_T^2 \quad (4)$$

$$v = \frac{E}{2G} - 1 \quad (5)$$

The fracture toughness (K_{Ic}) was determined by means of the single-edge precrack beam (SEPB), following the experimental procedure given in [12], with some adjustment for the precracking detection to non-transparent materials (present situation) that are detailed in ref. [13]. In the SEPB method, rectangular beam (x axis) specimens, with final dimension of 3(broadness, B) × 4(width, W) × 25 mm, were cut from the pellets, and one face (3x25) is grinded and polished down to mirror finish using a 0.25 µm grade diamond paste. An indentation line consisting of up to 20 Vickers indents was performed on this latter face with a 9.81 N indentation load and a dwell of 5 s. The indented beam was then loaded in a bridge-flexure device, so as to develop a tensile stress normal to the indentation line. A precrack then forms at a critical value of the tensile stress (pop-in), which propagates until its front reaches the compressive upper part of the beam. An acoustic emission sensor was placed beside the lower support to detect the precrack pop-in sound. Once the sound was detected, the loading was immediately interrupted. The length of the obtained precrack (a) was checked so as to fulfil the ASTM standard requirements [14]. This is chiefly to ensure that the precrack is long enough to avoid some residual stress effects stemming from the Vickers indent and short enough to avoid artifacts from the upper "free" surface. The precracked beam was then fractured in three-point bending, with a span length (S) of 20 mm, and a cross-head speed of 2 µm·s^{-1}, small enough to record a complete load-displacement curve with over 20 data points on loading, but large enough to prevent stress corrosion due to the humidity in the ambient atmosphere [13]. In addition, two experiments were conducted with a cross-head speed of 0.02 µm·s^{-1}, on the WG and WG / SAED materials, in order to investigate the fracture properties (stress intensity factor, crack extension and crack opening displacement) by means of an image correlation technique (details below) for sake of comparison with the results extracted from the load-displacement curves.

Fracture toughness was calculated from the maximum applied load (F_{max}) in the three-point bending load-displacement curve:

$$K_{Ic} = \frac{F_{max}}{B\sqrt{W}} Y^*, \qquad with \;\; Y^* = \frac{3}{2}\frac{S}{W}\frac{\sqrt{\xi}}{(1-\xi)^{3/2}} f(\xi) \quad (6)$$

where $f(\xi) = A_0 + A_1 \xi + A_2 \xi^2 + A_3 \xi^3 + A_4 \xi^4 + A_5 \xi^5$ and $\xi = a/W$. The (A_0, A_1, A_2, A_3, A_4, A_5) coefficients are equal to (1.9109, − 5.1552, 12.6880, −19.5736, 15.9377, − 5.1454) respectively in the present case where $S/W \approx 5$.

However, in most cases, the chosen cross-head speed and the values for the relative precrack depth, ξ, resulted in an unstable fracture regime. As explained in ref. [13], this situation

is suitable for an accurate measurement of K_{Ic} but does not allow for a straightforward determination of the work of fracture from the area under the load-displacement curve.

Nevertheless, the fracture surface energy can be estimated from stress intensity-energy similarity principle:

$$\gamma = \frac{K_{Ic}^2}{2E'} \quad (7)$$

where E' is taken equal to $E/(1 - \nu^2)$ in plane strain.

Double cleavage drill compression tests (DCDC) [15] were carried out to study the crack path in-situ during crack extension. Parallelepipedic bars, 35(length)×3(width)×2(broadness) mm^3, were used for these experiments. A circular hole, 0.325 mm in diameter ($2R$), was drilled through the broadness of the plate, at the center of the 3x35 face, using a diamond drill. Note that whatever the shift of the hole to the center of the specimen, the crack extends along the median plane parallel to the 2×35 face. The DCDC specimens are loaded in compression under an optical microscope (VHX-5000, Keyence Ltd, Japan) on a micro mechanical testing machine (Deben Ltd, UK) at a displacement rate of 1 µm·s^{-1} until the onset of crack extension from the surface of the hole and in the longitudinal direction (i.e. aligned with the compression axis), which typically occurs for a load between 500 and 550 N (i.e. for a stress, σ, of about 87 MPa in average) and are then rapidly unloaded. The specimens are then re-loaded to investigate the re-opening of the existing cracks with a recording frame rate of 3 images per second up to 550 N (or 450 N for the WG / a-SiO_2 composite), and further loaded to 650 N (550 N for the WG / a-SiO_2 composite) at a rate of 0.5 µm·s^{-1} associated with an image recording rate of 4 Hz. When a load of 650 N is reached, this load is maintained for 2 min in order to observe possible slow crack propagation processes. The specimens are then unloaded at a rate of 1 µm·s^{-1}. This type of experiment is particularly well suited to monitoring cracking and to getting insight into the crack path, as crack propagate over a distance (a) that can exceed several mm, and as the crack velocity can be controlled by the applied compression force (F). However, the analysis of the stress field at the vicinity of the crack front in DCDC experiments is not straightforward. An analytical expression was proposed for the stress intensity factor in the opening mode when $6 \leq a/R_h \leq 12$ [16]:

$$K_I = \frac{\sigma\sqrt{R}}{1.595 + 0.353(\frac{a}{R_h})} \quad (8)$$

where σ, R_h and a are the compressive stress, the hole radius and the crack length respectively.

It is noteworthy that the far field compressive loading results in a uniform tangential stress along the crack plane, which is referred to as the T-stress (T), and may have a significant incidence on the critical K_I value, K_{Ic}, for crack extension. The T-stress corresponds to the second-order term of the Williams series [22]. For a crack in opening mode (I), it is noted T_I. If T_I predominates over K_I, which is the case for short cracks with respect to the hole radius, then crack extension is not solely governed by K_I and the stress biaxiality needs to be accounted for [17-19]. The ratio of the tangential stress in the crack plane and the normal stress is referred to as the biaxiality factor, β, and is expressed as:

$$\beta = \frac{T_I\sqrt{\pi a}}{K_I} \quad (9)$$

Using this expression, β can be interpreted as the ratio between the remote stress along the crack path and that normal to the crack path. In the case of a DCDC experiment, the T-stress is negative and intense (it may reach 90 % of the compressive stress when $a/R_h > 8$) and was

tabulated as a function of the specimen geometry in ref. [20]. Negative *T*-stress values are known to promote stable crack propagation.

3.3 Image correlation method

The evolution of K_I upon crack extension as well as the fracture toughness values (SEPB measurements) were also investigated by means of an image correlation technique. In this technique, a high contrast random speckle pattern was deposited on the surface of the specimens in a typically few mm large region including the crack, and the displacement field in the crack tip region was determined, using a high-resolution camera (28 Mpix, PROSILICA GT 6600) coupled with a x4 telecentric lens (TC16M009, Opto Engineering Corp.). Images recording (4 Hz) and mechanical loading were synchronized and the UFreckles software was used to get the displacement field [21], using 12 pixels size elements (1 pixel = 1.37 µm). The image resolution allowed to measure displacements as small as 10 nm (Fig. 5) considering a typical uncertainty of 0.01 pixel.

The analytical solution proposed by Williams [22] for the displacement (planar solution for a crack in a linear elastic medium) was then used to model the experimental data and after optimization of the coefficients in the William series, by means of a standard minimization routine (least squares calculation) that is illustrated in Fig. 5 in the case of a SEPB precracked specimen made of the WG / SAED composite. Values for K_{Ic} (first order term) and for the *T*-stress (second-order term) associated with the DCDC test were derived for cracks extending over a few mm (Figs 6a to 6d). In addition, some DCDC experiments were carried out in-situ in an X-ray tomograph (Figs 6e to 6g and next paragraph) and further analyzed by DVC. Williams series were again used to determine K_I and T_I stress distributions along the front of the equivalent crack. These latter experiments were performed on the WG / SAED and WG / B_2S_3 grades, which offer the advantage of a significant X-ray absorption contrast between particles and matrix, so that particles act as a natural volume speckle allowing the determination of the volume displacement field (see [23] for details).

3.4 X-Ray Tomography

In-situ mechanical experiments in a X-ray tomograph were carried out in a laboratory scale micro-tomograph (Phœnix X-ray, V | tome | X; more details in [24]). The tension and intensity of the X-ray tube were set at 80 kV and 280 µA, respectively. This configuration results in a conical X-ray beam and the resolution of the observations depends on the distance between the imaged sample and the source. In the present case, a compact DCDC testing machine was placed as close as possible to the X-ray tube, leading to a voxel size of 2.5 µm (Fig. 6i). At the selected intensity and voltage, the spot size of the X-ray tube is known for being smaller than 2.5 µm. It can then be certified that the geometric blus is negligible in our reconstructed volumes. The exposure time for a given projection was 500 ms. For each angle, the image used for the volume reconstruction is the average over three successive equivalent projections. The 3D image reconstruction was performed by means of the datos | x2 (Phœnix X-ray) software by means of a filtered back-projection algorithm. 1920×1920×1536 pixels^3 volumes were obtained at increasing values of the applied load during the compression to perform the DCDC test. In order to limit crack propagation during the substantial amount of time required to acquire the radiographs, the load was increased to 550 N and then immediately decreased by 50 N and maintained constant for 55 min. In a second step, the load was increased again to 600 N, followed by a rapid decrease to 550 N and a 55 min plateau at this load. The final step consisted in reloading to 650 N, followed by a rapid decrease of the load to 600 N and a 135 min long plateau at this load. The data acquisition started after 15 min during the load plateau, that is

after crack stabilization, and lasted 40 min. With these experimental specifications, an overall of 5 images were recorded for three different load plateaus.

4. Results

4.1 Fracture toughness (SEPB test) and fracture energy

The load-displacement curves obtained on precracked bending bars according to the SEPB method specifications are shown in Fig. 7. The relative initial crack length (a/W) is between 0.36 and 0.55 in all cases and, for a cross-head speed of 2 μm·s^{-1}, unstable crack propagation is observed but for the final "tearing" of the remaining ligament at $a/W > 0.7$ leading to complete fracture (Fig. 7). The dotted lines in Fig. 7 show the range in which the data could not be recorded because the crcak propagated too quickly and are extrapolated from the final tearing stage in order to catch up with the unstable regime (vertical straight segments). This situation prevents the measurement of the overall work of fracture and thus of the actual fracture surface energy. Nevertheless, accurate and environment-independent K_{Ic} values can be calculated from the peak load by means of Eq. (6) (straight through notch in a bending bar) (Table 3). It turns out that the presence of a second phase does not always improve the fracture toughness. K_{Ic} is significantly enhanced in the case of a-SiO_2 and SAED additions, but is almost unaffected by the incorporation of B_2S_3 and is slightly decreased in the case of BZBa particles. These results will be discussed in § 4.2 in view of the details of the crack path and the values for K_{Ic} of the individual phases.

Two stable crack extension SEPB experiments were performed using a cross-head speed of 0.02 μm·s^{-1}, one on the sintered window glass and the other on a WG / SAED composite specimen (Fig. 9). For these experiments, the displacement along the x-axis in a region encompassing the crack was continuously monitored during crack extension by means of a speckle pattern (paint) deposited at the surface of the beam (xz plane). Three crack extension stages, numbered ①, ② and ③ in Fig. 9, were identified. In the first stage, the precrack front opens but its extension remains undetectable. A displacement jump, associated to a force drop, is sometimes observed as the precrack closes just after the precracking step on the bridge-flexure device, and thus needs to be re-opened before extension on the bending device (see ref. [12] for details). This was not the case for the tested specimens used for the stable crack extension experiments. In the second stage, as soon as K_I reaches 0.4 MPa·m$^{0.5}$, the crack propagates in a non-uniform manner, so as to reach a situation where the front line becomes straight and normal to the vertical axis (z axis), which corresponds to a uniform σ_{xx} opening stress. This alignment of the crack front results in a very limited crack extension on the right-hand side, but none on the left-hand side of the bar. Then, in the third stage, as K_I reaches 0.58 MPa·m$^{0.5}$ (from Williams series modelling), the straight crack starts to extend stably and uniformly. Therefore, K_{Ic} as obtained from the Williams series modelling is about 0.58 MPa·m$^{0.5}$. K_{Ic} as obtained with the peak load is about 0.65 MPa·m$^{0.5}$ and is in agreement with the value reported for the unstable test in Table 3 (0.67 MPa·m$^{0.5}$). Note that the crack front goes out of the range of the image correlation technique when its length becomes larger than 3.2 mm. The area under the load-displacement curve allows the determination of the work of fracture. The ratio of this work to the fracture surface area results in a fracture surface energy, γ, of 2.5 J·m^{-2}. This value is a bit smaller than the ones reported in Table 3 and calculated from K_{Ic} or obtained in a similar test on an ordinary window glass (bulk) [12]. In this latter case, $\gamma = 2.8$ J·m^{-2}. This difference corroborates the fact that the fracture surface energy of a sintered window glass is a bit smaller (Table 3), likely because the interfaces between the glass "grains" is enriched in moisture (and possibly slightly contaminated with carbon) and provide a weaker path for the crack. It is noteworthy that the influence of moisture (stress-corrosion process) becomes more and more important as the loading rate is decreased.

In the case of the WG / SAED composite, the influence of the particles on the stable SEPB test is very significant and makes the analysis difficult. As the crack opens during loading, jumps in the crack front position and in the stress intensity factor are observed (Figs 9e,f), between 0 and 0.2 MPa·m$^{0.5}$, which correspond to pinning and depinning events. Then, the displacement field determined at the surface by means of image correlation might differ significantly with the one inside the material as the stress field at the vicinity of a particle is different in the bulk and at the surface. The crack front exhibits many curved segments resulting from the interaction with the particles. Successive pinning and depinning events are responsible for the plateau observed during the stable extension regime (regime ②) in Figs 9b and 9c and correspond to the extension of the crack from the first crack arrest line and to the second one in Fig. 9d). Unfortunately, the crack length was already too large at this point to allow the projection on the Williams series. Values of 0.25 and 0.35 MPa·m$^{0.5}$ were derived for K_{Ic} from the image correlation method (lateral surface) and from the peak load respectively. The fracture surface energy as derived from the work of fracture is about 1.8 J·m^{-2}. These values of K_{Ic} and γ are much smaller than the one determined with the unstable SEPB test (Table 3) and suggest a determining influence of moisture in this composite. Further investigations are necessary to get insight into the role of water in the presence of $SrAl_2O_4$ particles.

4.2 DCDC experiments

During the second loading stage of the DCDC specimen, that is after the first cycle aimed at initiating cracks from the hole, there is almost no crack extension while K_I and T_I, as determined from image correlation at the surface (xz plane) keep increasing (Fig. 10a to 10c). At the onset of crack extension, for a load over 450 N, K_I reaches a critical value, K_I^*, which is reported in Table 4. A comparison of these values of K_I^* corresponding to a crack extension regime and typically associated with the 3 to 4.5 min time interval, with the fracture toughness is relevant. The values of K_I^* are much larger than the K_{Ic} values measured by the SEPB method but for the WG / BZBa composite. In this latter case, the very small K_I values (Fig. 10b) might be attributed to the chemistry at particle / particle interfaces (presence of moisture and residual carbon?), but this calls for further investigations.

The crack extension velocity just after the onset of crack extension is in-between 0.15 and 17 µm·s^{-1}. In the present case, experiments were performed in a humid environment with a moisture content of about 60 %. In such a case, according to the stress-corrosion cracking diagram [12, 26], the crack velocity interval would correspond to a stress intensity ranging between 0.45 and 0.58 MPa.m$^{0.5}$ (region drawn in red in Fig. 11). For sake of comparison, the K_I and β values as obtained from the approximate formulae given by Eqs (8, 9) and the T_I stress as determined in the theoretical analysis provided in ref. [19], are also reported in Table 4. The values of K_I obtained with Eq. (8) are between 0.34 (WG) and 0.38 (WG / SAED) and are much smaller (but for the WG / BZBa grade) than the ones derived from image correlation analysis performed at the surface of the specimens, while the T values are quite in agreement and the β values are much larger (in absolute values). The T stress is between – 78 and – 96 MPa and the biaxiality index, β, ranges between – 15 and – 30 for all materials. Although the reasons for the differences between the data obtained from the observations at the surface of the loaded specimens and those resulting from the theoretical analysis remain to be elucidated, it is anticipated that the presence of a tortuous crack front and out-of plane excursions, as well as secondary order microstructural stress fields at particle sites, bring to light the limits of the kinematics (image and volume correlation) ↔ static analogy in the case of such material and mechanical complexities, as is discussed in § 5. Furthermore, the stress intensity values resulting from the analytical expression, which range from 0.32 to 0.38 MPa·m$^{0.5}$, that is about half of the SEPB values obtained during high velocity unstable experiments, suggest that the influence of moisture is very important in the present case.

The distributions of the crack length, K_I, T_I and β along the crack front were studied in the case of the WG / B_2S_3 and WG / SAED composites by means of in-situ DCDC experiments in a laboratory scale X-ray tomograph and the results are shown in Fig. 12. The acquired volumes were analyzed by Digital Volume Correlation using Ufreckles. Unfortunately, The X-ray contrast between the particles and the matrix was too small for the other grades. However, this couple of experiments, showing for the first time the shape of cracks in a DCDC experiment of a bulk glass brings a few extra information, especially on the crack shape, compared to what can be observed form a surface. As expected, the crack position is extremely difficult to detect by naked eye from the grey level images, but it is revealed very clearly but the powerful DVC analysis (see for instance figure 6i). Cross-sections in the *yz* plane containing the reconstructed crack front (red lines in Fig. 12b) can then be easily extracted. They show indeed that the crack front is tortuous, and that its shape is rather wavy. The measurements also clearly show that the crack front is less tortuous in the case of B_2S_3 particles than in the case of SAED ones, consistently with the fact that the influence of B_2S_3 particles on the crack path is weak (see § 4.3). Still, the crack front line consists of segments with different orientations that are found to scale with the interparticle distance, so that the projection on the Williams series is found to capture the composite nature of the materials. It turns out that although the overall crack extension is clear in Figs 12c and 12e, the lines associated with the crack length as the acquisition time increases intersect at different points. This is likely because bridging and pinning phenomena occurring at the crack front affect the displacement field to such an extent that projection onto a Williams' series based on homogeneous linear elastic materials is not accurate. This is probably the reason for the observed crossing of the curves. Nevertheless, we verified that the crack front line derived from the Williams' series was parallel to the isocountour strain line (an xx strain component of 0.01 was chosen), supporting the analysis. The overall crack extension as the load is increased from 500 to 600 N with plateaus at 500, 550 and 600 N, and the crack length distribution along the front is illustrated in Figs 12c and 12e respectively for the WG / B_2S_3 and WG / SAED composites. Interestingly, short areas where the crack is the shorter are associated with peaks in the stress intensity factor (Figs 12d and 12f) and vice-versa. This is consistent with the fact that particles are obstacles that hinder crack propagation and hence result in a larger crack opening (locally), which corresponds to a larger K_I value. The K_I fluctuations along the crack front are typically of the order of 0.5 to 1 MPa·m$^{0.5}$ for the WG / B_2S_3 grade and of 1 to 2 MPa·m$^{0.5}$ for the WG / SAED one, and are related to the fine details of the crack path and of the microstructural stress state in the materials, as discussed in § 5.

4.3 Fracture path

The fracture path was investigated by in situ observation of the surface of the specimen during the final stable crack extension stage in the SEPB experiments in cases where such a stage could be observed (Figs. 7 and 8f), which provide in-plane (*yz* plane) views of the fracture surface (Figs 8c to 8f). Post-mortem observations of the fracture surface complete these investigations. In addition, observations were made on DCDC specimens, allowing for much larger crack extension range, and better image resolution. In this later case, the crack is watched from the side of the specimen, normal to the fracture surface (Figs 13-15).

In the case of the WG / a-SiO_2 composite, relatively large residual stresses are predicted (Table 2), and the tangential normal stress, $\sigma_{\theta\theta}$ (hoop component; polar coordinates), in the matrix at the vicinity of a particle is positive. In such a situation, a propagating crack tends to be attracted towards the particles, especially since during external loading, the Poisson's ratio mismatch is also favorable to the attraction of the crack front by the particles (Fig. 1). As a result, the crack front is twisted and deflected on approaching particles and a tortuous fracture surface follows. The crack further goes through the particles thanks to the perfect chemical

bonding between WG and a-SiO_2, which leaves fractured particles on the fracture surface (Fig. 13a).

In the case of the WG / BZBa and WG / B_2S_3 composites, Poisson's ratio is much larger for the particles ($\nu_i \sim 0.28$-0.29) than for the matrix ($\nu_i \sim 0.23$) and, as expected from the theoretical analysis which results are depicted in Fig. 1, no crack pinning or bridging is expected. Indeed, nearly straight cracks are observed from the side (DCDC specimens; Figs 15b,c), while in-plane observations show only a slight tortuosity, especially in the case of B_2S_3 particles (SEPB specimens; Fig. 13b,c). Particles are mostly broken along the fracture surface in the WG / B_2S_3 grade. BZBa particles seem to have no incidence on the crack path (Fig. 15b) and a straight and rather flat fracture surface is observed in the WG / BZBa composite (Fig. 13b).

In the case of the WG / SAED composite, a pronounced pinning of the crack front by the ceramic particles is observed, which shows up i) by the curved segments of the crack front as it extends by means of a jerky, intermittent process (Fig. 9f), and ii) by the numerous lines in arcs of circles connecting adjacent particles left on the fracture surface after the sudden depinning of the crack front on loading (Fig. 13d). Besides, some wake hackle marks looking like small secondary cracks are visible at particle sites. These marks are aligned with the main crack extension direction and are located at the border of the particles in a plane (*xz* plane) normal to the one of the main crack (*yz* plane), along the same "vertical" direction (*z* axis). Wake hackle results from the interaction of an advancing crack with elastic singularities. When the crack front splits at the particle site, the two fronts can cross the obstacle on slightly different planes, creating a step or "tail" that fades as the main crack goes away from the obstacle [27]. This phenomenon is observed in the WG / SAED composite and to a lesser extent (less visible) in the case of a-SiO_2 particles. Furthermore, in the case of particles that are stiffer and stronger than the matrix, residual stresses accumulate when the pinning particles are set in tension at the crack front. This situation was described by Evans [28]. Since the deformation of a particle is smaller than the one of the matrix upon loading thanks to much larger elastic moduli for the particles, as the particles are loaded in the *x* direction (normal to the precrack plane) some second-order σ_{yy} stress component takes birth at the surface of the particle. This second-order (microstructural) stress is favorable to opening a crack in the *xz* plane. In this composite, as the crack extends through a particle, it follows the easy cleavage planes of the $SrAl_2O_4$ crystal, so that intragranular steps are observed on the fracture surface (Fig. 15d).

The different situations encountered in the investigated glass matrix / glass particles composites are shown in Fig. 15. Cracks are attracted by the a-SiO_2 particles, which are ultimately crossed most of the time. B_2S_3 and BZBa induce nearly no visible effect on the crack propagation and SAED particles tend to pin the crack lips and to induce a pronounce crack front curvature in-between pinning particles. This latter effect is visible in the *yz* plane, ie normal to Fig. 15. As a crack penetrates a SAED particle it benefits from the superior toughness of this ceramic phase and is constrained by the orientation of the easy cleavage plane (intragranular deflections).

5. Discussion

5.1 Microstructural stress state

The understanding of the fracture behavior of a composite material requires the knowledge of the micro-heterogeneous stress state at the vicinity of the particles, the interfacial bonding and the second phase physical properties. Whereas the first plays a key role on the crack path in the matrix, the second determines the crack-particle interactions and the third allows to estimate the inherent particle contribution to the effective toughness of the composite (provided the crack extends across the particle). Secondary order stresses result from i) the processing cycle, and in

particular the thermally-induced strain stemming from the thermal contraction mismatch between the matrix and the particles upon cooling from the glass transition temperature (viscous relaxation is almost ineffective below this temperature), and ii) the far field loading as the stress state becomes heterogeneous in the neighborhood of particles due to elastic property mismatch.

An analytical form for this latter contribution was proposed by Evans [29] considering an elastic spherical inclusion (G_i, ν_i) of radius R in an elastic matrix (G_m, ν_m) loaded in tension (far field stress σ_∞). Although the case of a DCDC experiment is more complicated as a compressive load is applied to induce a tensile stress in the transverse direction, which results in a biaxial stress field acting on the crack front, Evans'model provides some general features regarding the crack/particle interaction in the case of an elastic property mismatch. For a loading along the x axis, the maximum normal stress σ_{xx} at the surface of a particle on a diametral plane ($x = 0$ for an inclusion centered on the origin) is expressed as:

$$\sigma_{xx}\,(x = 0) = \sigma_\infty + 2\,\sigma_\infty\,[A(R/y)^2 + 3B(R/y)^4] \quad (10)$$

where $A = [(1-2\nu_i)\,G_m - (1-2\nu_m)\,G_i] / [4(1-2\nu_i)G_m + 4G_i]$ and $B = [G_m - G_i] / [4G_m + (3-4\nu_m)G_i]$

Therefore, the second-order stress arising from the elastic property mismatch exhibits a maximum of $\Delta\sigma_{xx}(x = 0, y = \pm R)$ of $2\,\sigma_\infty\,(A+3B)$. Taking a far field stress of 100 MPa (typical order of the stress applied in DCDC experiments), values for of 0.25, – 4.3, 4.6 and – 21 MPa were calculated for the WG / a-SiO_2, WG / BZBa, WG / B_2S_3 and WG / SAED composite respectively. A positive value corresponds to a tensile hoop stress contribution (tangential normal stress) and thus to an attraction of a crack toward the inclusion, while a negative value favors crack deflection around the inclusion. In the case of a thermal expansion mismatch, the tangential normal stress acting normal to the y axis in the x direction, and hence of interest for a crack approaching a particle in a $x = 0$ diametral plane and extending in opening mode, is expressed as [8]:

$$\sigma_{xx}\,(x = 0) = \sigma_\infty + (P/2)(R/y)^3 \quad (11)$$

When values stemming from the thermal expansion mismatch pressure (P in table 2) are compared to those of the elastic mismatch (taking $y = R$), it appears that the thermal effect is much larger in all cases but for the WG / SAED composite. In this latter material, both thermal and elastic property mismatches should drive the crack to bypass the particles. Nevertheless, the fractured surface observations reveal that a crack propagates along a rather flat surface, with pinning-depinning events and crack front bowing in-between pinning particles, ultimately resulting in particle cleavage. This means that the driving force for a crack to extend normal to the far field loading axis and to propagate in the opening mode (mode I) prevails over the second order stresses that build up at particle sites. A similar situation is observed in the WG / B_2S_3 grade, where in spite of a negative pressure (P) and a positive $\Delta\sigma_{xx}$ increment arising upon loading due to the elastic property mismatch, which both are expected to drive a propagating crack toward the particles, the fracture surface is relatively flat and shows fractured particles. Nevertheless, the thermal stress seems to have a pronounced effect on the crack path in the case of the WG / a-SiO_2 composite, where the large value of P induces crack front attraction and further trapping at particle sites.

5.2 Local stress intensity factor and toughening mechanism

When the (homogeneous) hydrostatic stress inside the particles, P in Eq. (1), is negative, a propagating crack tends to be attracted toward the particles and experiences an effective stress intensity factor (K_{Ieff}) larger than that due to the far field stress ($K_{I\infty}$). An expression for K_{Ieff} was proposed by Krstic and Khaund [30] in the case of a crack approaching a particle along its diametral plane normal to the far field loading axis:

$$K_{Ieff} = K_{I\infty} - PR^3/r^{5/2} \text{ (for } r > R\text{)} \quad (12)$$

where again R is the particle radius and r is the distance to the particle center.

This is a transient effect as the crack will then be pinned or trapped at particle site and may either extend through the particle or bypass it depending on the shape and on the relative toughness of the particle (K_{Ici}/K_{Icm}). In the case where the crack is pinned and particles ultimately cleaved, such as for the WG / SAED composite, the crack front arches between two adjacent and pinning particles as observed in Fig. 13d. Therefore, during crack growth (that is when $K_{Ieff} = K_{Ic}$ is satisfied along the crack front), K_I typically experiences variations from $K_{I\infty} - PR^{1/2}$ to K_{Ici}. This results in an intermittent and heterogeneous crack extension process, which is illustrated in Figs 12c and 12d. SAED particles having a toughness of 4 MPa·m$^{0.5}$ are expected to induce the largest variations of K_I among all particles tested in our study. Considering a particle radius of 20 μm and a pressure of 7.9 MPa (Table 2), one obtains a reduction of the stress intensity factor by about 0.04 MPa·m$^{0.5}$, which is negligible. In contrast, in the case of the WG / a-SiO_2 grade, the stress intensity variation is of 1.12 MPa·m$^{0.5}$ and is positive, which makes the crack extension easier. Note that in this latter case, the actual stress intensity factor in the matrix near the surface of the inclusions is greater than the glass fracture toughness, so that microcracking should be observed upon cooling, especially at the vicinity of the largest particles. Since no microcracking was observed, it is anticipated that either the hydrostatic stress in the particles as estimated from Eq. (1) is overestimated, or 2) particles don't act as defects and are free of large flaws or propagating cracks in their neighborhoods, so that the strength in the volume is governed by the cohesive strength which is of the order of several GPa (strength measured on pristine glass fibers in the absence of surface flaws [31]).

Then, the variation of K_I along the crack front upon crack extension scales with the difference between K_{Ici} (inclusions) and K_{Icm} (matrix). When SAED particles are incorporated, this gives a 3.3 MPa·m$^{0.5}$ interval, which is in agreement with the fluctuations recorded in Fig. 12f. The fluctuation of K_I observed for the WG / B_2S_3 grade (Fig. 12d) are smaller as the microstructure is more homogeneous (finer and better dispersed inclusions). In this latter case, fractured particles were observed on the fracture surface and both thermal expansion and elastic property mismatches are expected to drive the crack front toward the particles. But the effect should be limited, and the fracture surface is almost flat.

The fracture toughness of a-SiO_2 is about the same as the one of the matrix, and the toughness of B_2S_3 and BZBa is smaller. Therefore, it is not expected that the crossing of particles affects the toughness much, but should lead to a slight decrease for B_2S_3 and BZBa particles. The major source of change is due to the crack path tortuosity induced by the particles, with contributions from the particle geometrical characteristics (size and shape) and from the microstructural stress state.

In the case of the WG / a-SiO_2 composite, the constituent materials of both the matrix and the particles have the same toughness (~ 0.7 MPa·m$^{0.5}$). Therefore, the toughening effect is likely to result from the increase of the fracture surface area due to multiple out-of-plane crack excursions. A series of pictures extracted from a video of a propagating crack, as observed during a DCDC experiment, illustrate this process (Fig. 14). Nevertheless, as many particles are left broken on the fracture surface, the intrinsic strength of the a-SiO_2 particles might come into play, and it is anticipated that the strength of the silica beads, which are almost defect-free (the flame synthesis method results in a flawless "polished like" surface), is much larger than the one of the glass matrix. Besides, the resistance to crack propagation at the matrix / particle interface might also bring some toughening contribution. These latter effects have not been explored so far.

In the case of the WG / B_2S_3 composite, the toughness of B_2S_3 (K_{Ic}=0.57 MPa·m$^{0.5}$) is smaller than the toughness of the window glass (K_{Ic}=0.67 MPa·m$^{0.5}$). Therefore, fractured B_2S_3 particles are expected to reduce the overall fracture energy. The fact that the toughness of the WG / B_2S_3 composite is similar to the one of the sintered window glass is likely to stem i) from the slight crack deflection induced by the Poisson's ratio mismatch ($\nu_i > \nu_m$) and the corresponding increase of fracture surface area through the WG glass matrix, and ii) from the strength of the particles, which, as for the other flame-synthesized beads, is probably much larger than the one of the matrix.

In the case of SAED particles, which are much tougher and stiffer than the matrix, as K_{Ici} / K_{Icm} is smaller than 5, the theoretical 3D approach proposed by Bower and Ortiz [32] predicts that one particle at the most should bridge the crack walls, that is there is a single line of pinning particles along the crack front. With a particle volume fraction V_p of 7 %, the toughness of the composite should be about 10 % larger than the one of the matrix, which gives a value of 0.8 MPa·m$^{0.5}$. This is smaller than the actual toughness of the composite, equal to 0.94 MPa·m$^{0.5}$. This difference might stem either from the additional toughening contribution resulting from the intragranular crack deflection process (along easy cleavage planes) or from the existence of second-order stresses that are decreasing the stress intensity at the vicinity of the particles (as discussed above). Note that in the WG / SAED composite, the increase of the fracture toughness, K_{Ic}/K_{Icm}=1.4, is very close to the values reported by Swearengen et al. [33] for a comparable volume fraction of alumina particles in a glass (K_{Ic}/K_{Icm} between 1.4 and 1.54), in spite of the fact that in this latter case the authors claim that fracture rarely propagates through the inclusions. In a recent study [34] based on the estimation of the variations of the stress intensity factors arising from geometrical perturbations of the crack front, regardless of second-order stresses at particle sites, and assuming that both matrix and inclusions share the same elastic moduli, it was concluded that in the case where K_{Ici} / K_{Icm} is larger than 4, the crack should systematically bypass the inclusions, hence preventing both bowing and bridging phenomena. In such a situation, the intrinsic toughness of the second phase does not come into play in the effective toughness of the composite. Nevertheless, crack front bowing in-between particles and crack front pinning are clearly observed in the WG / SAED composite, which shows that the elastic property mismatch plays a key role in this problem. A rule of mixture accounting for the surface fraction of the particle, taken as $V_s=V_p^{2/3}$=3.7 % assuming a randomly orientated plane, and the fracture surface energy of both phases can be used to estimate the toughness of the composite, provided all particles are fractured in a given fracture plane. This can be written:

$$\gamma = (1 - V_s)\, \gamma_m + V_s\, \gamma_i \quad (13)$$

Taking the experimental γ_m and values from Table 3, one obtains a fracture surface energy of 5.8 J·m^{-2}. The corresponding value for the fracture toughness, as calculated with Eq. (7), is 0.95 MPa·m$^{0.5}$, which is in remarkable agreement with the experimental result. Results and discussion for each composite grade are summarized in table 5.

5.3 *T*-stress and sensitivity to biaxiality

The compressive stress that accompanies DCDC experiments, of the order of – 100 MPa, is responsible for the remarkably large *T*-stresses acting on the crack, ranging between – 40 and – 100 MPa, and to biaxiality factors that can reach about –20 to –30 in the worst cases, i.e. for the WG / B_2S_3 and WG / SAED composites. In such a situation, differences in the mode I fracture properties might be observed between SEPB, which only involves opening stresses normal to the crack plane, and DCDC experiments. This is probably because glasses exhibit some tension / compression asymmetrical behavior regarding their mechanical properties (elasticity and strength in particular) favoring the development of bulk dissipation under

compressive loadings. Besides, the presence of inclusions with different Poisson's ratio makes the analysis of DCDC experiments very complicated, especially for large biaxiality factors. Although observations of the crack trace at the surface on DCDC specimens and further analysis of the displacement field led to the largest toughness for the WG / a-SiO_2 and WG / SAED composites, in agreement with SEPB measurements, critical K_I values much larger than those obtained by the SEPB method are obtained. This illustrates the limits of the equivalence between the static (analytical formulas using load measurement) and kinematics (Williams displacement field) approaches when the geometry of the fracture surface and the actual material behavior depart from the fundamental hypothesis at the source of the Williams' analytical expressions. In these cases, the analysis of stress (by measuring the load and the closed-form solution) or strain (by projecting the measured kinematic field onto the Williams series) intensity factors is no more equivalent. Considering an equivalent K_I (in terms of strain energy density) as the algebraic average of both stress (issue from load) and strain (issue from DIC) intensity factors would allow to incorporate bulk dissipation within the evaluation of the glasses toughness. Bulk dissipation being promoted under compressive loading, this might explain the increase of the resulting equivalent fracture toughness observed under extreme biaxiality factors. The presence of second phase particles associated with second-order micro-stress fields, resulting in a tortuous crack path and in a non linear crack front, is also a critical issue which calls for further theoretical investigations.

6. Conclusion

Dense particulate composites with homogeneously dispersed glass beads (7 vol. %) made of three different glasses in a soda-lime-silica glass matrix were obtained by means of flame synthesis (beads) and further consolidation by the spark plasma sintering technique. In addition, a composite was prepared by incorporating 7 vol. % $SrAl_2O_4$ particles in the same matrix.

The fracture toughness of the glass matrix was increased by ≈ 40 % by incorporating 7 vol. % silica glass particles, while retaining transparency. This toughening is likely to stem from the crack front trapping and pinning phenomena at the a-SiO_2 particle sites and from the resulting tortuosity of the crack path. A similar improvement is observed when 7 vol. % $SrAl_2O_4$ particles are incorporated, which results in a translucent material. In this latter case, the toughening is due to the crack passing through the particles and thus making the large fracture surface energy of the ceramic particles come into play. In-situ slow crack growth experiments (DCDC) in a X-ray tomograph revealed large variations of the crack length and of the stress intensity factor along the crack front, which corroborate the occurrence of trapping / pinning / depinning events, and is consistent with the arched lines observed on the fracture surface. In the case of barium aluminosilicate glass (B_2S_3) beads, a propagating crack either extends across the particles (mostly) or avoids particles, which leads to a slightly tortuous fracture surface. The crack is almost straight and ignores the second phase particles in the case of zinc barium borate glass (BZBa) particles.

It is concluded that the thermal expansion mismatch plays a key role when a-SiO_2 particles are added to a window glass, while the strength and toughness of the ceramic particles is responsible for the toughening effect when $SrAl_2O_4$ particles are incorporated. In all cases the incidence of Poisson's ratio mismatch on the fracture behavior of the studied particulate composites is light, if any. The problem of a crack propagating through a brittle particulate composite with thermal and elastic property mismatches is difficult and in-depth quantitative modeling is required to go further on interpretation. Besides, the very large influence of the *T*-stress and the sensitivity of glass to biaxiality should be taken into account to provide a sensible modeling of the DCDC test. The sensitivity of glass to biaxiality, which can be expressed severely in the case of DCDC experiments, is probably the origin of the significant differences between the fracture characteristics measured by the SEPB and DCDC experiments.

Acknowledgements

The European Research Council is greatly acknowledged for the Advanced Grant 320506 (DAMREG) of the 7th framework program "Ideas".

References

[1] T. Lacondemine, C. Roux-Langlois and T. Rouxel, Role of Poisson's ratio mismatch on the crack path in glass matrix particulate composites, Inter. J. Fract. 207（2017）73-85.
[2] T. Rouxel, Elastic properties and short-to-medium range order in glasses, J. Am. Ceram. Soc., 90 (10) (2007) 3019-3039.
[3] J. Moriceau, P. Houizot, T. To, A. Mougari, H. Orain, et al., Nucleation and crystallization of $Ba_2Si_3O_8$ spherulites in a barium aluminum silicate glass, and mechanical properties of the obtained glass-ceramics, J. of the Europ. Ceram. Soc. 41(1) (2021) 838-848.
[4] M. Dubernet, E. Bruyer, Y. Gueguen, P. Houizot, J.C. Hameline, X. Rocquefelte & T. Rouxel, Mechanics and physics of a glass/particles photonic sponge, Sci. Reports (2020) 10:19495.
[5] W. Ströber, A. Fink and E. Bohn, Controlled growth of monodispersed silica spheres in the micron size range, J. Colloid and Interface Science 26 (1) (1968) 62-69.
[6] P. Larionau, M. Hujova, M. Michalková, M. Mahmoud, A. Švančárková, D. Galusková, M. Parchoviansky, E. Bernardo, D. Galusek, J. Kraxner, J. Low-alkali borosilicate glass microspheres from waste cullet prepared by flame synthesis, International Journal of Applied Glass Science 12 (4) (2021) 562-569.
[7] A. Bertrand, J. Carreaud, G. Delaizir, J.R. Duclère, M. Colas, J. Cornette, M. Vandenhende, V. Couderc, P. Thomas, A Comprehensive Study of the Carbon Contamination in Tellurite Glasses and Glass-Ceramics Sintered by Spark Plasma Sintering (SPS), J. Am. Ceram. Soc. 97 (2014) 163-172.
[8] E.M. Rabinovich, Preparation of glass by sintering, J. Mat. Sci. 20 (12) (1985) 4259-4297.
[9] J. Selsing, Internal stresses in ceramics, J. Am. Ceram. Soc. 144(8) (1961) 419.
[10] R.W. Davidge and T.J. Green, The strength of two-phase ceramic / glass materials, J. Mat. Sci. 3 (6) (1968) 629-634.
[11] T. Rouxel, Fracture surface energy and toughness of inorganic glasses, Scripta Mat. 137 (2017) 109-113.
[12] T. Nose, T. Fuji, Evaluation of Fracture Toughness for Ceramic Materials by a Single Edge Precracked Beam Method, J. Am. Ceram. Soc. 71 (1988) 328-333.
[13] T. To, F. Célarie, C. Roux-Langlois, A. Bazin, Y. Gueguen, H. Orain, M. Le Fur, V. Burgaud, T. Rouxel, Fracture toughness, fracture energy and slow crack growth of glass as investigated by the Single-Edge Precracked Beam (SEPB) and Chevron - Notched Beam (CNB) methods, Acta Mater. 146 (2018) 1-11.
[14] ASTM C1421-10, Standard Test Methods for Determination of Fracture Toughness of Advanced Ceramics at Ambient Temperature, ASTM International, West Conshohocken, PA, (2010).
[15] C. Janssen, Specimen for fracture mechanics studies on glass, Rev. Phys. Appl. (Paris), 12 (5) (1977) 803.
[16] T.A. Michalske, W.L. Smith, and E.P. Chen, Stress intensity calibration for the double cleavage drilled compression specimen, Engng Fract. Mech., 45(5) (1993) 637-642.
[17] W.E. Warren, Theoretical analysis of the double cleavage drilled compression specimen, Intern. J. Fract., 33 (3) (1987) 223-235.
[18] K. Sedighiani, J. Mosayebnejad, H. Ehsasi, and H.R. Sahraei, The effect of *T*-stress on the brittle fracture under mixed mode loading, Procedia Engin., 10 (2011) 774-779.

[19] M.R. Ayatollahi and B. Saboori, *T*-stress effects in mixed mode I/II/III brittle fracture, Engin. Fract. Mech., 144 (2015) 32-45.
[20] T. Fett, G. Rizzi, and D. Munz, *T*-stress solution for DCDC specimens, Eng. Fract. Mech., 72(1) (2005) 145-149.
[21] J. Réthoré, Ufreckles, 2018. Available from: https://doi.org/10.5281/zenodo.1433776.
[22] M.L. Williams, On the stress distribution at the base of a stationary crack, J. Appl. Mech., 24 (1) (1956) 109-114.
[23] T. Lacondemine, J. Rethore, E. Maire, F. Celarie, P. Houizot, C. Roux-Langlois, C.M. Schleputz and T. Rouxel, T, Direct observation of the displacement field and microcracking in a glass by means of X-ray tomography during in situ Vickers indentation experiment, Acta Mat., 179 (2019) 424-433.
[24] J.Y. Buffiere, E. Maire, J. Adrien, J.P. Masse, E. Boller, In situ experiments with X ray tomography: an attractive tool for experimental mechanics. Experimental mechanics, 50 (2010) 289-305.
[25] M. Szutkowska, Fracture toughness of advanced alumina ceramics and alumina matrix composites used for cutting tool edges, J. of Achievements in Mat. And Manufacturing Engineering, 54 (2) (2012) 202-210.
[26] S.M. Wiederhorn, Influence of water vapor on crack propagation in soda-lime glass, J. of the Amer. Ceram. Soc., 50(8) (1967) 407-414.
[27] G.D. Quinn, "Fractography of Ceramics and Glasses", NIST special Publication 960-16e2 (2016) p. 5-33.
[28] A.G. Evans, Structural reliability: A processing-dependent phenomenon, J. Amer. Ceram. Soc., 65 (3) (1982) 127-137.
[29] A.G. Evans, The role of inclusions in the fracture of ceramic materials, J. Mat. Sci., 9 (1974) 1145-1152.
[30] V. Krstic and A. Khaund, Conditions for toughening of particulate brittle composites, in "Advances in Fracture Research", (D. François Editor, Pergamon Press) vol. 4 (1981) 1577-1585.
[31] R. Kurkjian, P.K. Gupta, R.K. Brow, and N. Lower, The intrinsic strength and fatigue of oxide glasses, J. Non-Cryst. Solids, 316 (2003) 114-124.
[32] A.F. Bower and M. Ortiz, A three-dimensional analysis of crack trapping and bridging by tough particles, J. Mech. Phys. Solids, 39 (1991) 815-858.
[33] J. C. Swearengen, E. K. Beauchamp. and R. J. Eagan, Fracture Toughness of Reinforced Glasses, in "Fracture Mechanics of Ceramics", (Edited by R. C. Bradt, D. P. H. Hasselman, and F. F. Lange, Plenum, New York) vol. 4 (1978) 973-87.
[34] M. Lebihain, J.B. Leblond and L. Ponson, Effective toughness of periodic heterogeneous materials: the effect of out-of-plane excursions of cracks, J. Mech. Phys. Solids, 137 (2020) 103876.

Table 1

Physical properties of the glass grades and SAED ceramic particles. (*un*: undefined; *nd*: not determined). ν and n are Poisson's ratio and the refractive index respectively. Note that the elastic properties were measured on the parent bulk glasses used for particle manufacturing.

Ref.	ρ ($g \cdot cm^{-3}$) ± 0.02	T_g (°C) ± 3	$\alpha_{100\text{-}500\ °C}$ ($10^{-6} \cdot °C^{-1}$) ± 0.1	E (GPa) ± 1	G (GPa) ± 1	ν ± 0.01	n ± 0.002
a-SiO_2	2.20	≈1190	0.6	73	31.5	0.16	1.457
WG	2.50	564	9.0	73	29.7	0.23	1.519
BZBa	3.44	554	8.1	77	30.1	0.28	1.624
B_2S_3	3.99	717	11	67	26.0	0.29	*nd*
SAED	3.5	*un*	9.2	102	41.5	0.23	*un*

Table 2

Physical properties of the glass matrix particulate composites containing 7 vol.% second phase particles, as measured on 50 mm in diameter and 5 mm in thickness disks. The hydrostatic stress inside the particles, P, and the critical particle radius R_c, were obtained from Eqs. (1) & (2) respectively.

Matrix / inclusions	ρ ($g \cdot cm^{-3}$) ± 0.02	E (GPa) ± 1	G (GPa) ± 1	ν ± 0.01	P (MPa) ± 1	R_c (μm) ± 2
WG / a-SiO_2	2.48	73.0	29.8	0.225	– 251	12.5
WG / BZBa	2.61	72.0	29.1	0.235	+ 65	222
WG / B_2S_3	2.57	73.0	29.6	0.235	– 60	282
WG / SAED	2.60	74.0	30.1	0.23	+ 7.9	1650

Table 3

[1)]Fracture toughness, K_{Ic} as deduced from the peak load in the unstable SEPB tests and corresponding fracture surface energy (γ) as calculated by means of Eq. (7). [2)]from [25].

Matrix / inclusions	a-SiO_2	WG	Sintered WG	BZBa	B_2S_3	SAED	WG / a-SiO_2	WG / BZBa	WG / B_2S_3	WG / SAED
K_{Ic} ($MPa \cdot m^{0.5}$) ±0.05[1)]	0.71	0.70	0.67	0.62	0.57	4[2)]	0.91	0.60	0.68	0.94
γ ($J \cdot m^{-2}$) ±0.05[1)]	3.38	3.18	2.91	2.30	2.22	74.3[2)]	5.38	2.36	2.99	5.65

Table 4

DCDC experiments. [1)]From image correlation at the surface (*xz* plane); [2)]From the analytical expressions (Eqs (8, 9) and ref. [19] for T_I). a and R_h are the crack length and the hole radius respectively.

Matrix / inclusions	a/R_h ± 0.1	σ (MPa) ± 0.1	[1)]K_I* (MPa·m$^{0.5}$) ± 0.1	[2)]K_I* (MPa·m$^{0.5}$) ± 0.1	[1)]T_I (MPa) ± 5	[2)]T_I (MPa) ± 5	[1)]β ± 3	[2)]β ± 3
WG	8.6	93.8	1.29	0.34	–71	–80	–5.5	–22
WG / a-SiO_2	6.2	83.9	1.60	0.37	–42	–71	–2.6	–15
WG / BZBa	8.0	91.6	0.27	0.35	– 68	–78	– 30	–20
WG / B_2S_3	11.1	104.8	0.76	0.32	–51	–89	–8.6	–29
WG / SAED	9.5	113.2	1.41	0.38	–82	–96	–6.6	–25

Table 5

Summary of the observations and toughening mechanisms.

Materials	Mismatches	Second-order stresses		Fracture surface	Crack path	K_{Ic}/K_{Icm}
		thermal	elastic			
WG / a-SiO_2	$\nu_i < \nu_m$ $\alpha_i < \alpha_m$ $E_i \approx E_m$	Major	Negligible	Tortuous, with fractured inclusions and wake patterns on the back of the inclusions	Strong attraction toward particles and significant deflection	1.36
WG / BZBa	$\nu_i > \nu_m$ $\alpha_i \leq \alpha_m$ $E_i \geq E_m$	Minor	Minor	Flat, with some porosity	Moderate deflection	0.93
WG / B_2S_3	$\nu_i > \nu_m$ $\alpha_i \geq \alpha_m$ $E_i \approx E_m$	Minor	Minor	Flat, with fractured inclusions	Almost straight	1.01
WG / SAED	$\nu_i = \nu_m$ $\alpha_i = \alpha_m$ $E_i > E_m$	Negligible	Major	Rather flat, with fractured particles and arched segments, as well as secondary microcracks on the back of the inclusions	Weak deflection and rough fracture surface	1.4

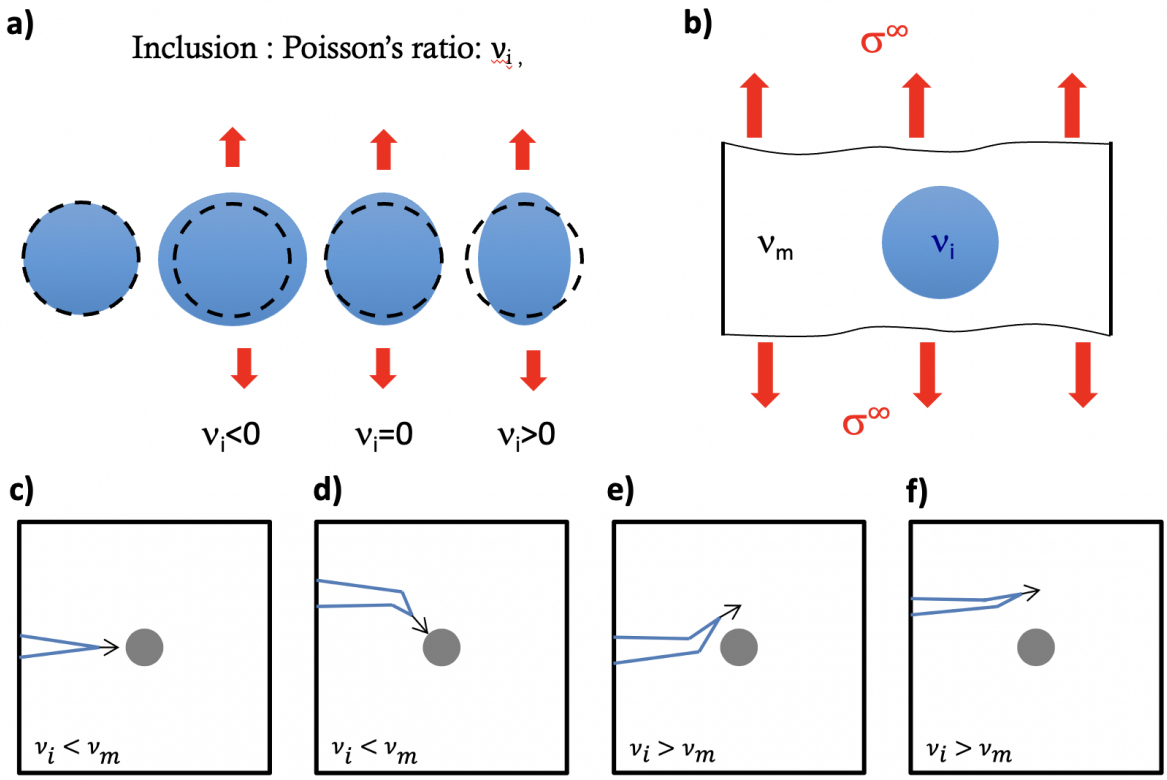

Fig. 1. schematic drawings of a) the deformation of an inclusion (dashed circle at rest) loaded in tension, b) an inclusion in a matrix loaded in tension (far field stress σ^∞ along the vertical axis), c) a crack approaching radially an inclusion for which $\nu_i<\nu_m$, d)) a crack attracted by an inclusion for which $\nu_i<\nu_m$, e) a crack being deflected by an inclusion for which $\nu_i>\nu_m$, and f) a crack propagating with a limited second-phase effect when $\nu_i>\nu_m$. Note that the situations depicted in c) to f) stem from theoretical analysis performed in ref. [1] for inclusions and matrices having the same Young's modulus.

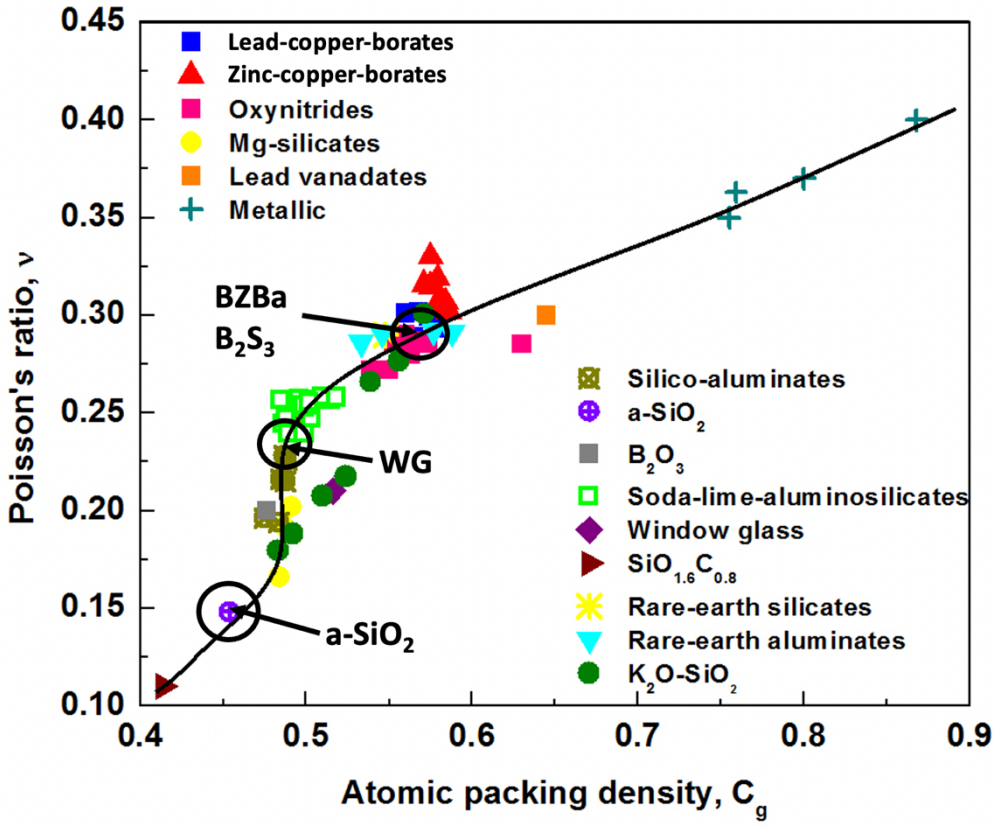

Fig. 2. Poisson's ratio of inorganic glasses. The four selected grades, referred to as a-SiO_2, WG, B_2S_3 and BZBa (see Table 1 for details) are within the black circles (extracted and augmented from Fig. 4 in [2]).

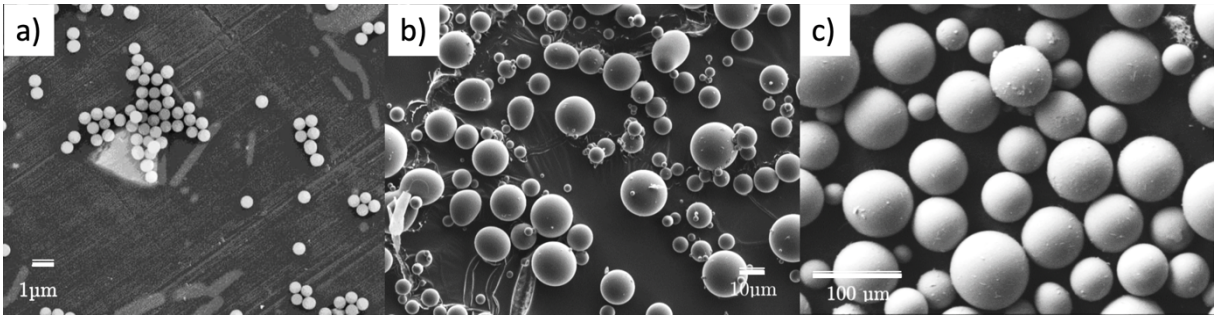

Fig. 3. Glass beads: a) a-SiO_2, Ströber process; b) a-SiO_2, flame synthesis; c) BZBa, flame synthesis.

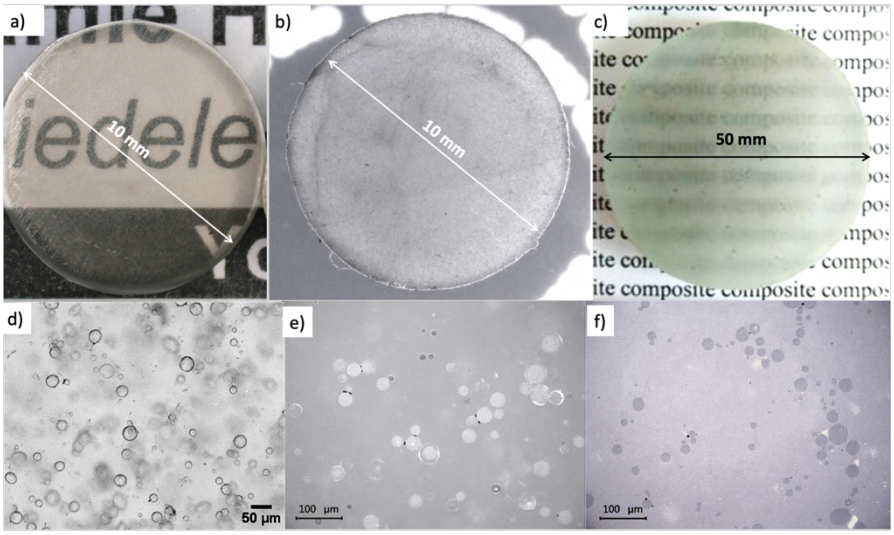

Fig. 4. a) Sintered BZBa pellet, 10 mm in diameter; b) sintered WG / a-SiO_2 (2 vol. %) composite, 10 mm in diameter; c) sintered WG / SAED (7 vol. %) composite, 50 mm in diameter; d) optical microscope image of a BZBa / a-SiO_2 (2 vol. %) composite; e) optical microscope image of a WG / B_2S_3 (7 vol. %) composite; f) optical microscope image of a WG / a-SiO_2 (7 vol. %) composite.

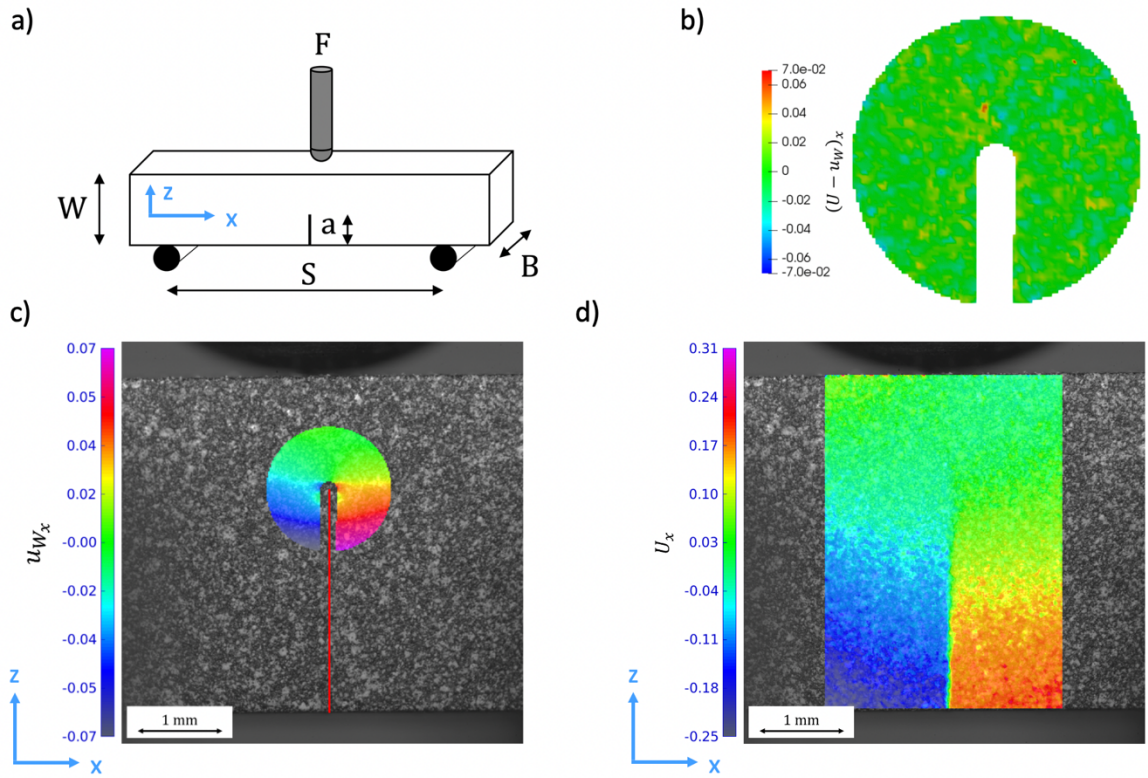

Fig. 5. a) Precracked beam for the SEPB testing technique; b) Residual for the *x* axis displacement component after minimization over the domain shown in c) for the WG / SAED specimen (the red line corresponds to the equivalent crack); d) Displacement along the *x* axis corresponding to the Williams series. Displacements are given in pixels (1 pixel = 1.37 µm).

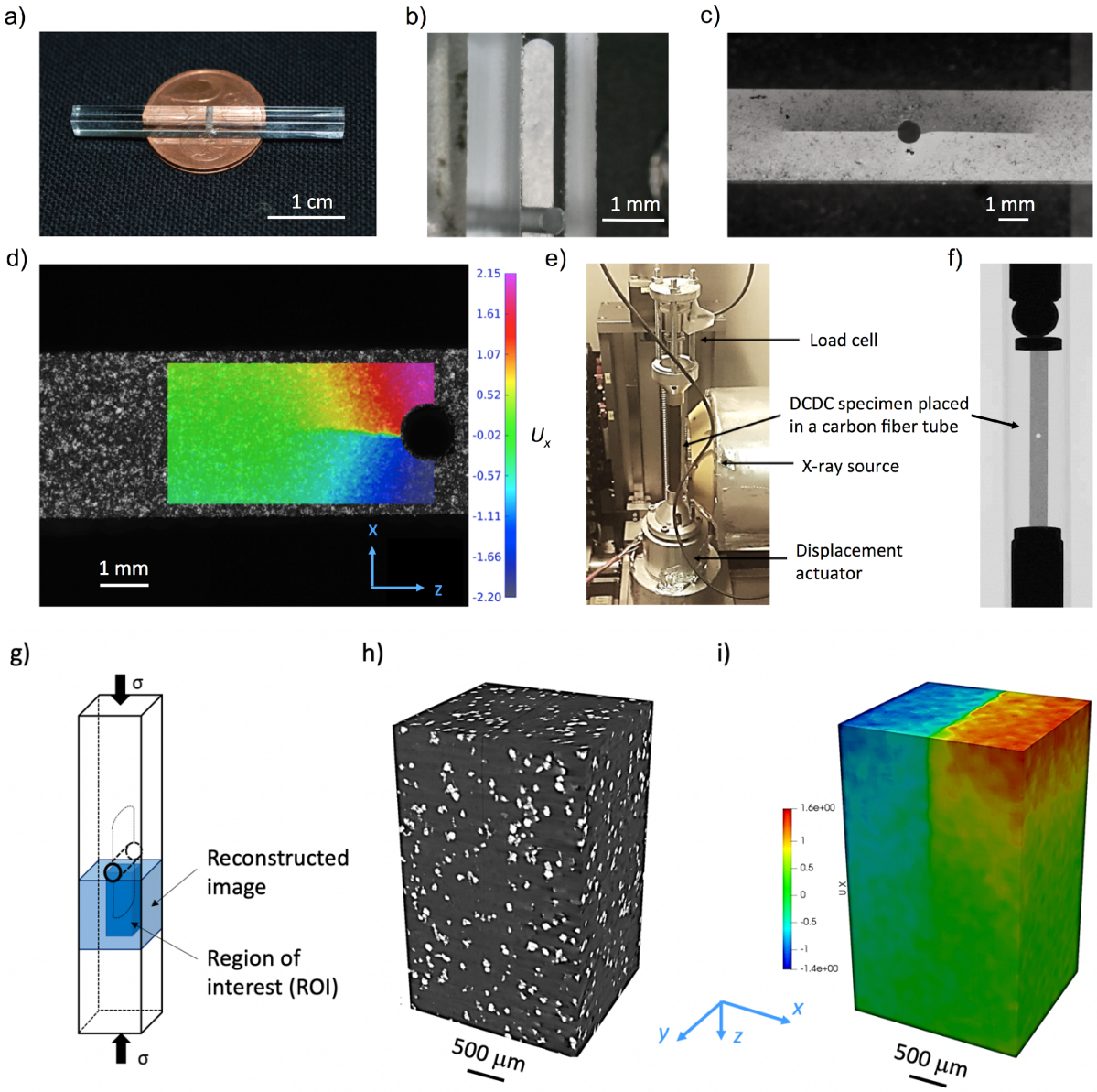

Fig. 6. a) Window glass DCDC specimen, with a 0.325 mm diameter hole at the center; b) After loading up to 550 N to induce a crack extension from the hole in the *yz* plane; c) *xz* plane view of cracks that propagated under a compressive load of 510 N in a WG / SAED composite specimen; d) Displacement component in pixels (1 pixel = 1.37 µm) in the *x* direction as measured at the surface (*xz* plane) by digital image correlation at the surface of a DCDC specimen (using a paint speckle pattern); e) The laboratory X-ray tomograph set-up equipped with a loading axis and showing a WG / SAED composite DCDC specimen during testing; f) The DCDC specimen inside the cylindrical chamber; g) Region of interest for the digital volume correlation; h) Reconstructed image in the case of WG / SAED DCDC specimen (glass matrix in dark grey and particles in white); and i) displacement component in voxels (1 voxel = 2.5 µm) in the *x* direction in the ROI at the vicinity of the crack front.

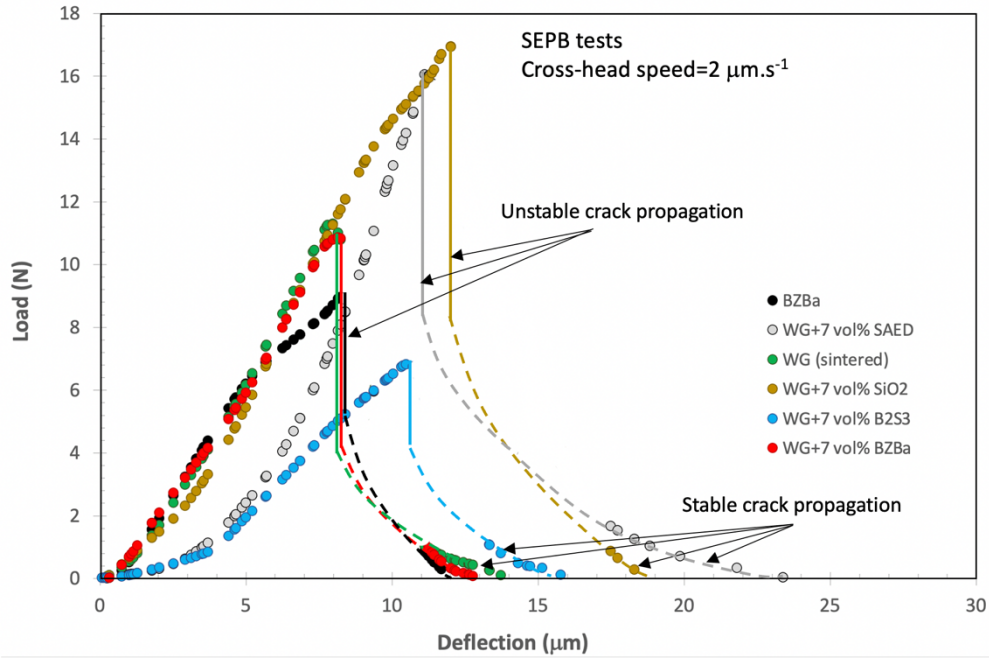

Fig. 7. Load-displacement curves obtained during the loading of the pre-cracked SEPB specimens in three-point bending. A displacement rate of 2 µm·s^{-1} was chosen. An unstable fracture regime is observed once the peak load is reached, followed by a stable fracture of the remaining ligament at $a/W > 0.7$.

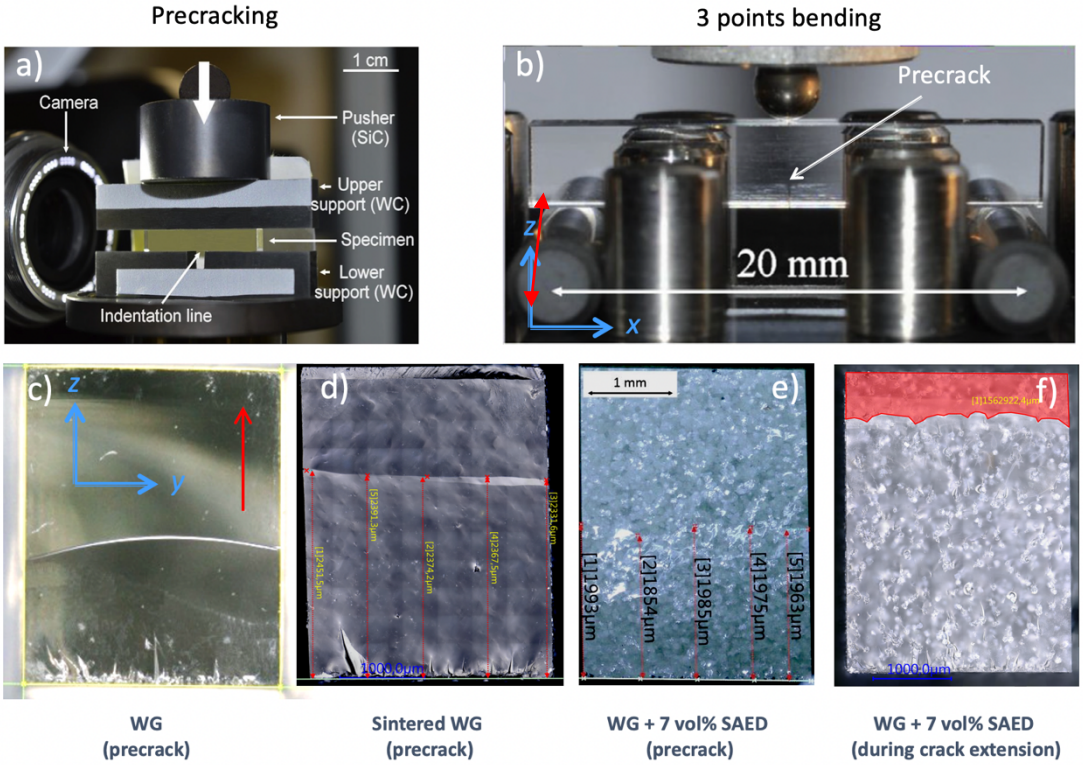

Fig. 8. SEPB testing. a) The precracking step, by means of a bridge-flexure anvil optimized to get a pop-in precrack with a/W between 0.35 and 0.6; b) the three-point bending test used to fracture the precracked SEPB bar. A precrack in c) a window glass (WG) (the red arrow indicates the crack extension direction) ; d) a sintered window glass; e) a WG / SAED (7 vol.%) composite. f) crack front during the final stable propagation stage through the remaining ligament (in red color) in a WG / SAED (7 vol.%) composite.

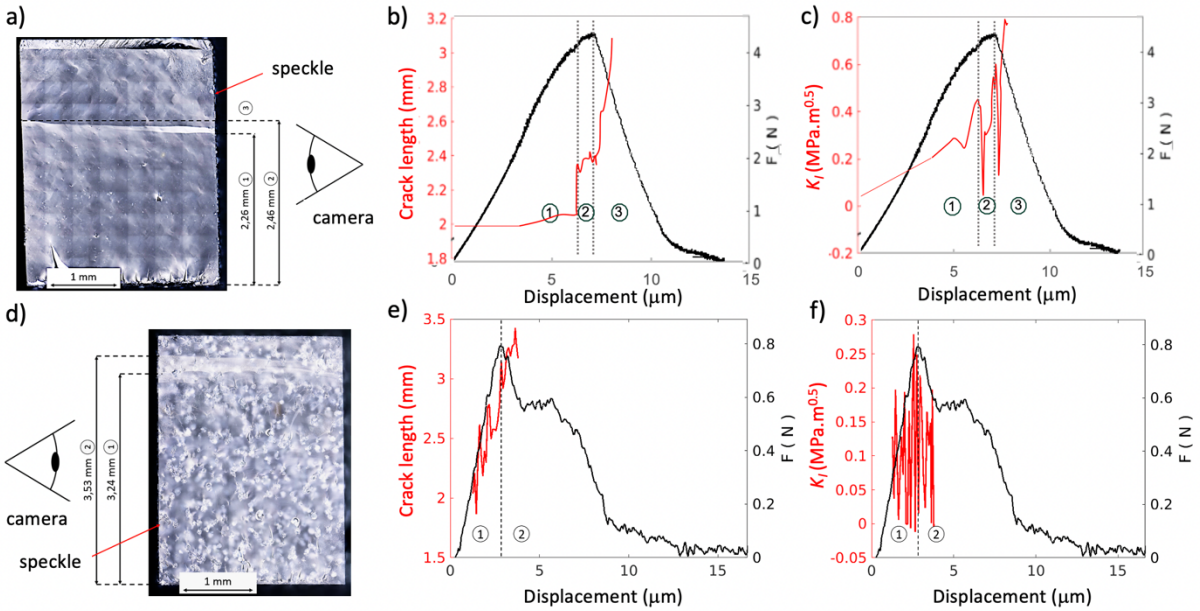

Fig. 9. Stable SEPB experiments. a) Sintered WG SEPB precracked specimen; b) Load-displacement curve (in black) and corresponding crack length (in red); c) Load-displacement curve and corresponding changes of K_I; d) WG / SAED composite precracked specimen; e) Load-displacement curve for the WG / SAED composite and corresponding crack length; f) Load-displacement curve for the WG / SAED composite and corresponding changes of K_I.

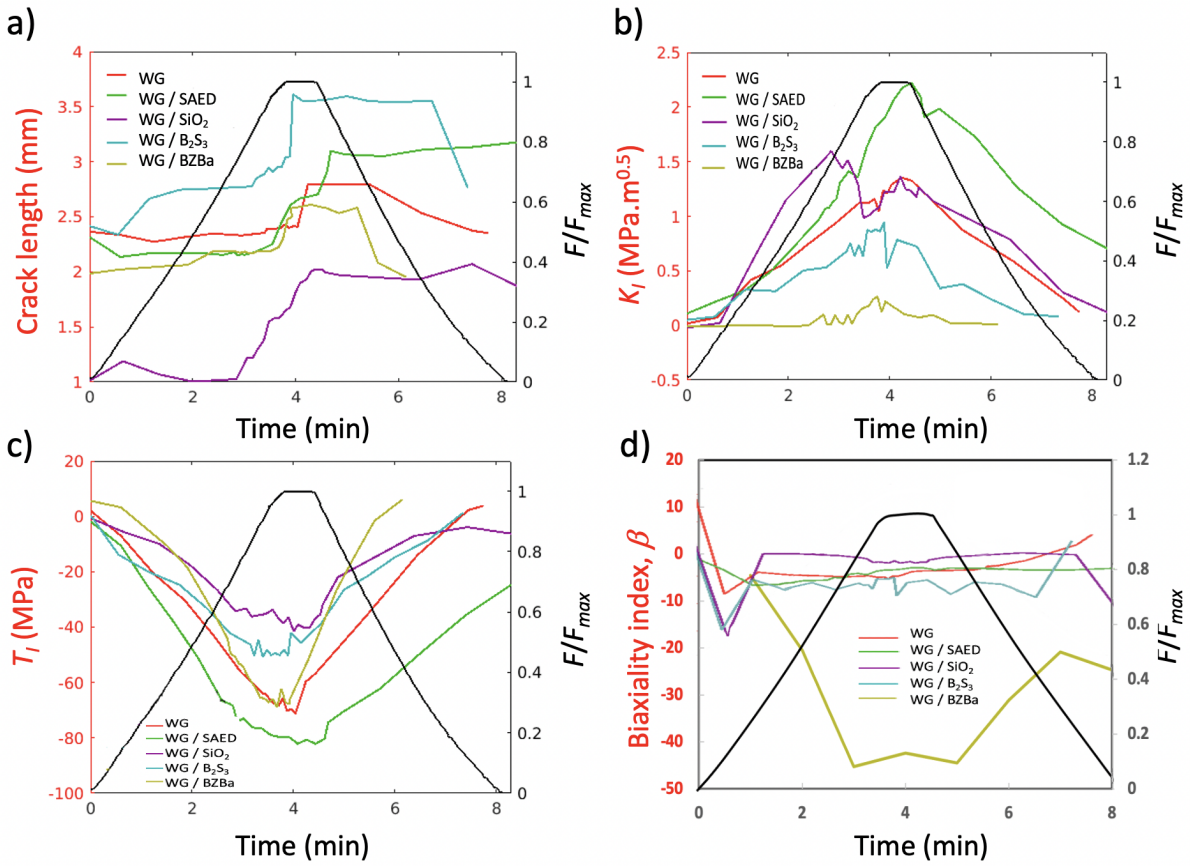

Fig. 10. DCDC experiments and corresponding evolution of a) the crack length, b) the stress intensity factor, K_I, c) the T stress, and d) the biaxiality factor, β, as derived from observations on the lateral surface (xz plane), and projections on the Williams series. The loading cycle is shown in black ink.

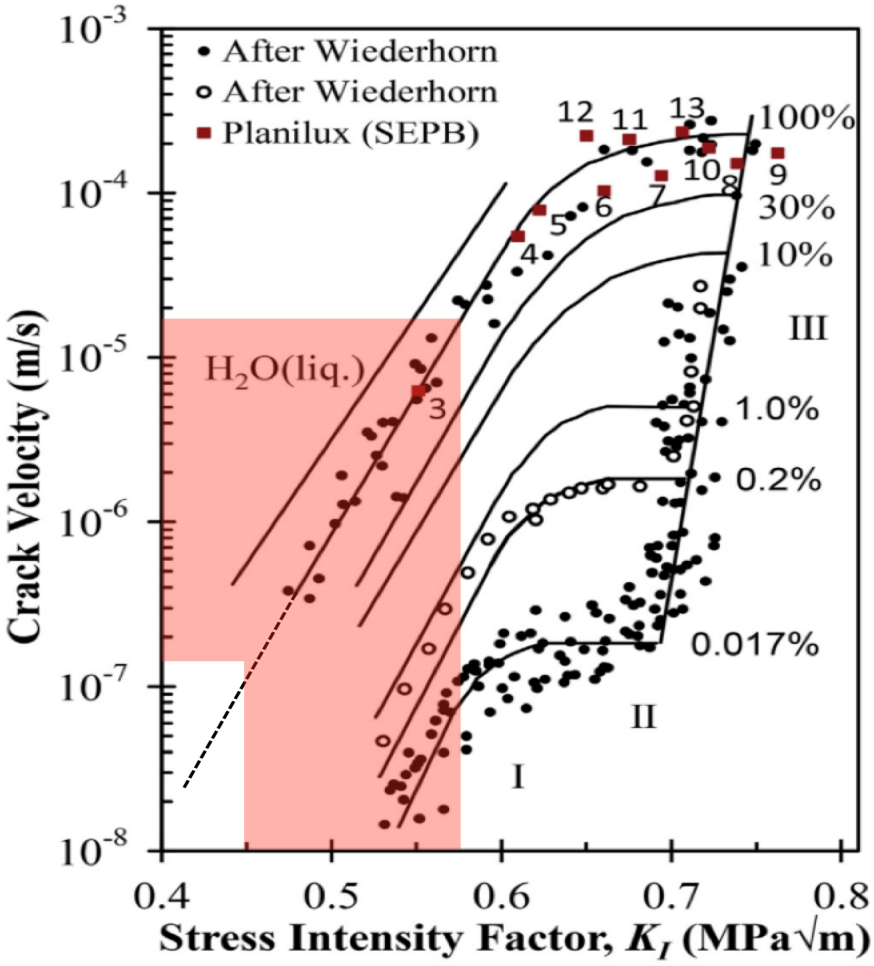

Fig. 11. Slow crack growth velocity in a window glass as a function of the stress intensity factor for different moisture levels. After Wiederhorn, [26], augmented with data stemming from SEPB experiments by To et al. [12].

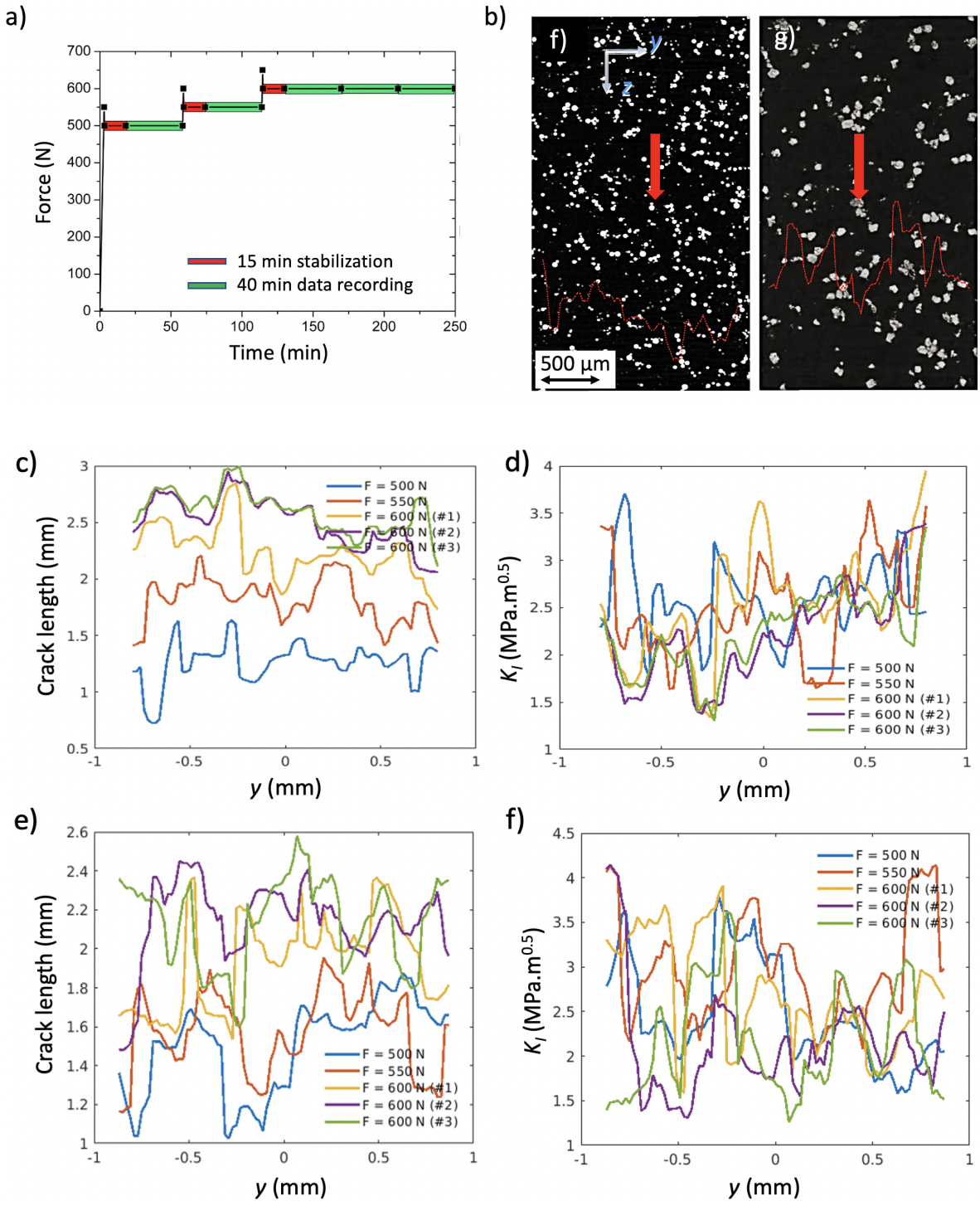

Fig. 12. DCDC experiments performed in-situ in the X-ray tomograph. a) Loading cycle corresponding to the recording of five 3D images; b) Tomographical cross-section in the *yz* plane showing the crack front (red line) as derived from the Williams series projections for the WG / B_2S_3 (left) and WG / SAED (right) grades respectively. The red arrows indicate the crack propagation direction; c) Crack length distribution along the crack front for the WG / B_2S_3 grade; d) Stress distribution along the crack front for the WG / B_2S_3 grade; e) Crack length distribution along the crack front for the WG / SAED grade; and f) Stress distribution along the crack front for the WG / SAED grade.

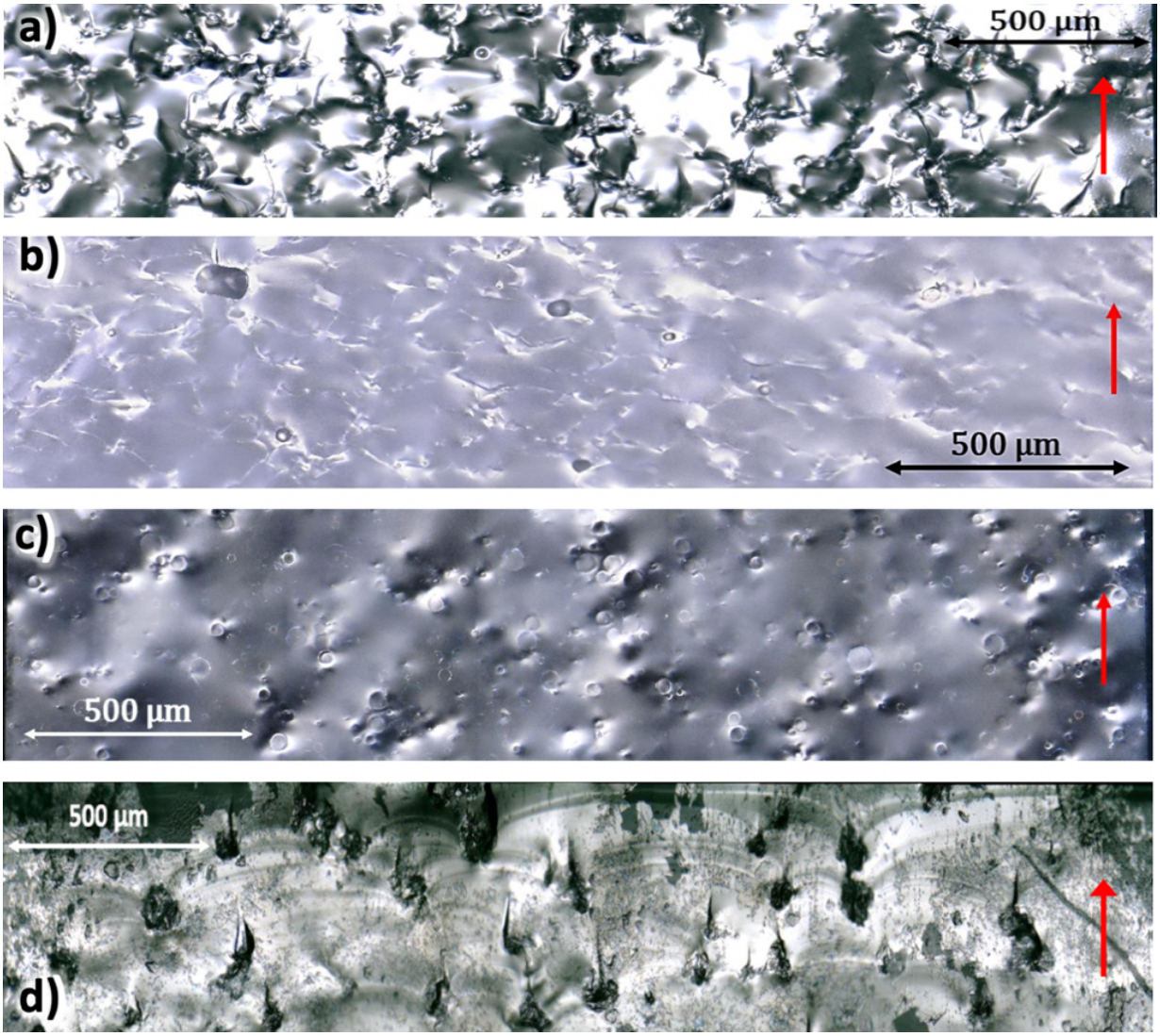

Fig. 13. Post-mortem fracture surface observations (optical microscope) associated with the unstable crack propagation (direction is indicated by the red arrows) resulting from SEPB experiments performed with a cross-head speed of 2 µm·s^{-1}. a) WG / a-SiO_2; b) WG / BZBa; c) WG / B_2S_3; d) WG / SAED.

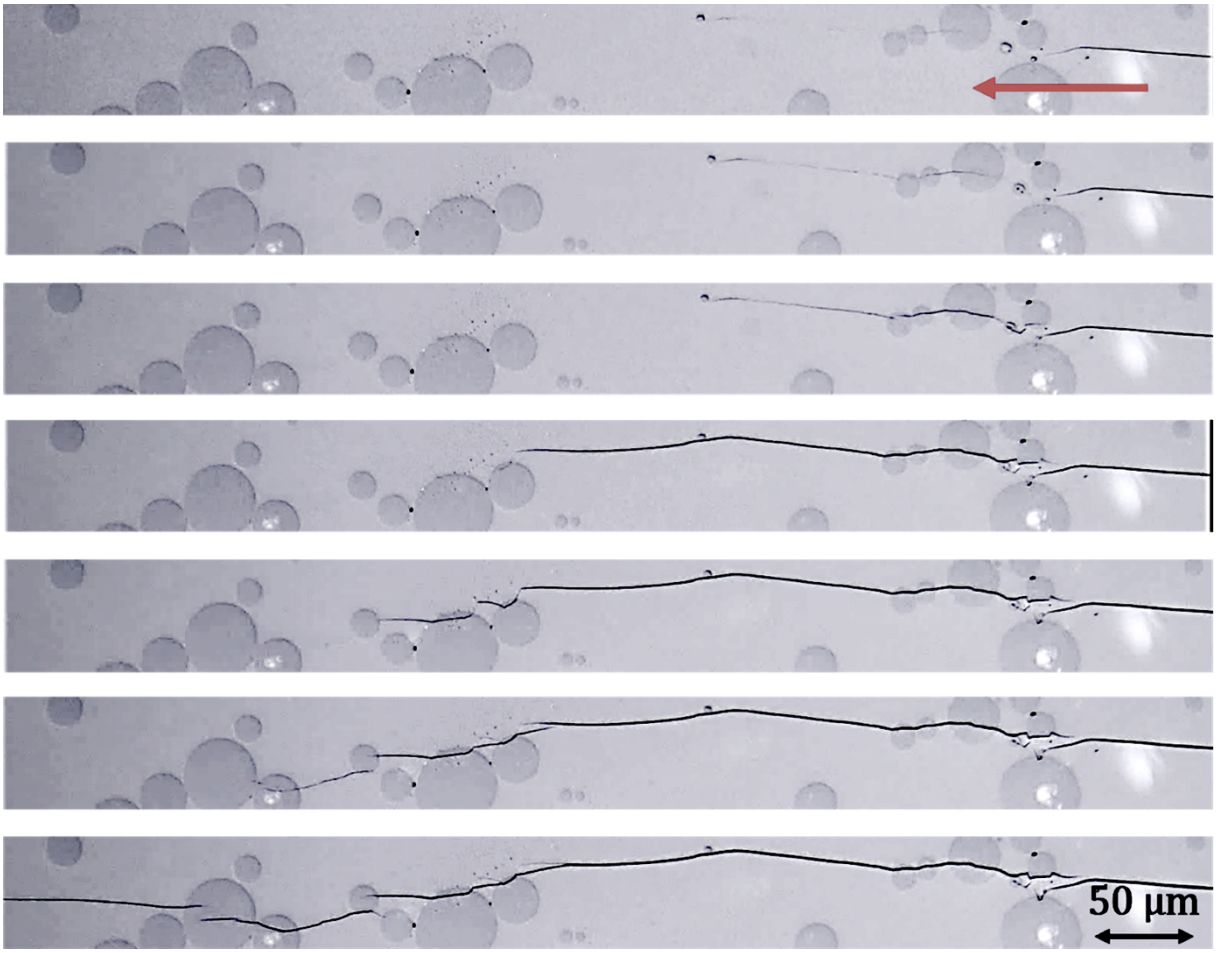

Fig. 14. A crack propagating in a WG / a-SiO_2 DCDC specimen (pictures extracted from a movie that can be seen at www.youtube.com/watch?v=cRF6ba2B4Wg). The mean crack velocity is about 0.01 mm·s^{-1}. The red arrow indicates the propagation direction.

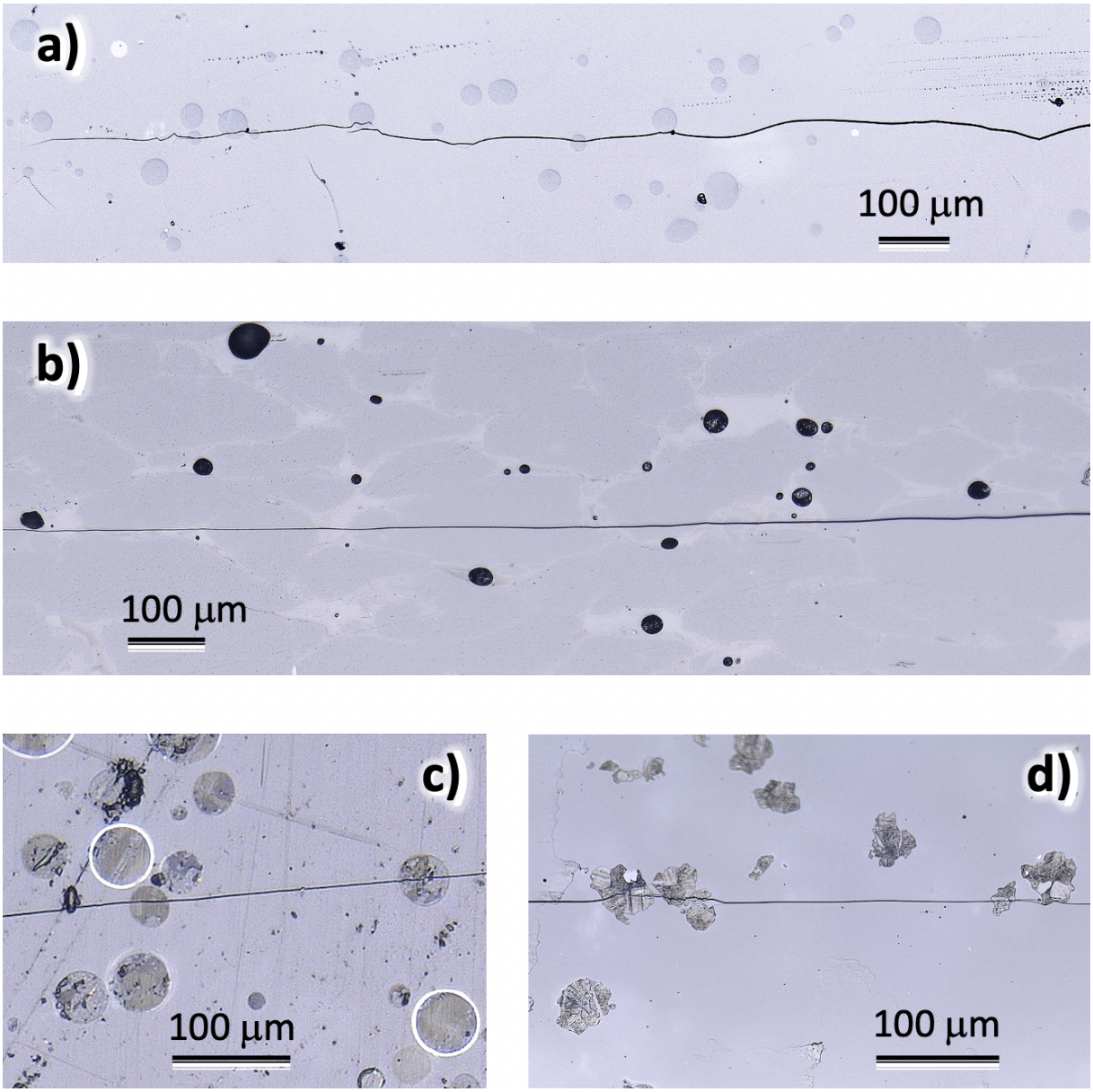

Fig. 15. Details of the crack path from the side observations during crack extension in DCDC specimens. a) WG /a-SiO_2; b) WG / BZBa; c) WG / B_2S_3; d) WG / SAED.